UNIVERSITY OF CALIFORNIA

Los Angeles

“Parametronics”- A New Way to Design Low Noise High Efficiency RF Microwave Front Ends

A dissertation submitted in partial satisfaction of the

requirements for the degree Doctor of Philosophy

in Electrical and Computer Engineering

by

Maziar Hedayati

2022

ABSTRACT OF THE DISSERTATION

"Parametronics"- A New Way to Design Low Noise High Efficiency RF Microwave Front Ends

by

Maziar Hedayati

Doctor of Philosophy in Electrical and Computer Engineering

University of California, Los Angeles, 2022

Professor Yuanxun Wang, Chair

The objective of this research is to develop, characterize, and demonstrate novel parametric architectures capable of wideband operation while maintaining high gain and low noise performance.

Parametric amplification is a process of RF-RF power conversion were well studied in the 1950s and 1960s that analyzed the power flow into and out of a nonlinear reactive element under excitation at its different harmonic frequencies. One of the most famous conclusions is Manley-Rowe relation that describes harmonics, intermodulation and how the energy transfer from one frequency to another frequency. Based on Manley-Rowe relation the energy transferred among different intermodulation can be configured to have different characteristics depend on the termination of intermodulation tons and harmonics. We will show, there are three different modes available: double sideband upconverting mode, negative resistance mode, and single sideband upconverting mode.

Based on the characteristics of each mode, we will design different parametric components by first developing a set of analytical models describing their achievable gain, noise figure and efficiency. These models will provide a set of design tools to design and optimize different prototype circuits. The prototype circuits will then be used to prove the concept based on gain, bandwidth, efficiency, and noise performance.

As the first design, we present a parametric downconverter that may be used in a mixer-first receiver front-end. In such a receiver, the first mixer should offer a satisfactory low noise figure (NF), high conversion gain (CG) to suppress the noise contribution of the next stages, and high linearity to avoid receiver saturation in the presence of interferences. Parametric mixers are known to offer parametric conversion gain for frequency upconversion with no fundamental noise penalty due to its parametric amplification nature. This work is the first experimental demonstration of a parametric downconverter that achieves positive gain and low noise figure. The proof-of-concept mixer with a center input frequency of 1.9 GHz and an output frequency of 1.45GHz is designed and implemented on PCB. The mixer achieves a measured peak conversion gain of 10 dB and a 1-dB compression point of +7 dBm. Furthermore, the fabricated mixer achieves a minimum noise figure of 2.8 dB over its bandwidth.

The second design is a novel matching technique for receivers with electrically small antenna (ESA) so that the receiver can achieve low noise performance over a broad bandwidth. We propose to match an electrically small dipole directly to a parametric amplifier, without using any inductors as they are often of low-quality factors and their loss contribute additional noise to the receiver. The parametric amplifier operates in a time-varying fashion, driven by a higher RF frequency pump. It exhibits a high impedance, time-varying capacitive load to the

ESA. Therefore, the low frequency voltage output from the ESA is detected at the input of the parametric amplifier, being amplified and upconverted to the proximity of the pump frequency at the output with minimum contamination of noise in this process. The proof-of-concept, a parametric matching for an electrically small bowtie dipole of ka<1/2 is designed and implemented on PCB which demonstrates that with this novel matching strategy, a low noise performance can be obtained for an electrically small antenna over wide bandwidth. The complete theory of parametric matching is also presented which has been validated with the nonlinear circuit simulation results.

A parametric power amplifier (PPA) with a unique load-modulation characteristic different from any existing architecture to enhance back-off efficiency will be presented as another application of parametronics. The proposed technique enables transmission of high peak-to-average-power ratio (PAPR) signals with high efficiency while maintaining excellent linearity. Analysis is conducted to explore the relationship between the proposed load modulation network (LMN) parameters and the performance of PA to achieve high back-off efficiency. Generalized design formulas of the LMN parameters are then introduced to study the total power delivering efficiency. Aided by the proposed load network, load modulation for class B amplifier can be achieved at saturation, leading to maximized efficiency over extended power. Upon theoretical proof of these discoveries, PA with a center frequency 220 MHz RF-input is developed and implemented on PCB. The prototype achieves 32 dBm output power, 49%–53% of efficiency at peak power and 49%–53% at 10-dB output back-off (OBO).

The dissertation of Maziar Hedayati is approved.

Danijela Cabric

Aydin Babakhani

Gregory J. Pottie

Yuanxun Wang, Committee Chair

University of California, Los Angeles

2022

This dissertation is dedicated to my God and my lovely family.

TABLE OF CONTENTS

ABSTRACT OF THE DISSERTATION ..... **ii**

TABLE OF CONTENTS ..... **vii**

LIST OF FIGURES ..... **ix**

LIST OF TABLES ..... **xi**

SYMBOLS AND ACRONYMS ..... **xii**

ACKNOWLEDGEMENTS ..... **xiii**

VITA ..... **xiv**

1 Parametric Amplification Background **1**

1.1 Theory Of Parametric Amplifiers 1

1.2 A Linear Time-Varying Property of a Non-Linear Capacitance 2

1.3 Dissertation Outline 5

2 Fundamentals Of Parametric Amplification and Mode Analysis **7**

3 Parametric Downconverter for Mixer-First Receiver Front-Ends **10**

3.1 Mixer-First Receiver Front-Ends Background 10

3.2 Theory 13

3.3 Stability Condition 18

3.4 Design Considerations 19

3.5 Measurement Results 23

4 Matching of Electrically Small Antennas for broadband, Low Noise Reception **26**

4.1 Electrically Small Antenna Matching Background 26
4.2 Motivation Of Matching Based on Parametric Amplification 27
4.3 ESA Matching with Parametric Amplifier Design 29
4.4 Experimental Characterization of The Parametric Matching 34
5 Parametric Power Amplifier for Extended Back-Off Efficiency 41
5.1 Background of Power Amplifier with Power Back-off Efficiency 41
5.2 Theory Of Parametric Load Modulator 44
5.3 Experimental Result 49
6 Summary 55
6.1 Conclusion 55
7 Appendix 57
8 References 68

LIST OF FIGURES

Figure 1.1: Circuit model for Manley and Rowe derivation. 2

Figure 1.2: Simplified circuit model for parametric circuit. 5

Figure 2.1: Three Parametric Amplification Modes – Lossless Cases. (a) Double sideband Upconverting Mode. (b) Negative Resistance Mode. (c) Single sideband Upconverting Mode. 9

Figure 3.1: Mixer-first receiver architecture. 13

Figure 3.2: Mixer gain and noise figure versus input quality factor. 17

Figure 3.3: Mixer gain and noise figure versus capacitance modulation index. 18

Figure 3.4: Equivalent circuit at signal frequency. 19

Figure 3.5: Stability region for downconverter. (a) Q_i=6, (b) Q_i=3. 19

Figure 3.6: Microstrip parametric down-converter mixer (a) Schematic. (b) Layout. 20

Figure 3.7: Input and output resonators (a) Single-port signal resonator. (b) Single-port idler resonator. 22

Figure 3.8: Capacitance-versus-voltage behavior of the varactor diode. 22

Figure 3.9: Fabricated microstrip parametric down-conversion mixer. 23

Figure 3.10: Measured and simulated gain and noise figure of the fabricated parametric mixer. 24

Figure 3.11: Measured and simulated output versus input power. 25

Figure 4.1. Parametric matching concept. 30

Figure 4.2. Electrically small dipole represented by an equivalent circuit model for TM_1 mode. 31

Figure 4.3. Simulation schematic of the matching circuit with the parametric amplifier designed for the electrically small antenna. 33

Figure 4.4. Simulated results of the parametric matching technique comparing to the theoretical prediction (a) gain (b) noise figure. 34
Figure 4.5. Simulated results of the parametric matching technique comparing to the theoretical prediction (a) gain (b) noise figure. 36
Figure 4.6. Parametric matching circuit design. (a) Multiple parallel bridge diode. (b) LO matching. (c) Interconnection between antenna and diode bridges. 36
Figure 4.7. Return loss from pump port. 37
Figure 4.8. The test setup. (a) Parametric matching. (b) Self resonance matching. 38
Figure 4.9. Fabricated antennas for measurement setup. Self-resonance antenna (Left). Unmatched electrically small bowtie antenna (Right) 38
Figure 4.10. The measured spectrum. (a) Self resonance matching. (b) Parametric matching. ... 40
Figure 4.11. Measured SNR improvements of the proposed parametric matching over self-resonance antenna. 40
Figure 5.1. Load modulation technique. 43
Figure 5.2. Circuit model of the load modulator. 44
Figure 5.3. Single sideband Upconverting Mode. 45
Figure 5.4. Microstrip parametric PA. (a) Schematic. (b) Layout. 50
Figure 5.5. Photograph of the stacked diode. (b)Capacitance-versus-voltage of the varactor diode. 51
Figure 5.6. Fabricated microstrip parametric power amplifier. 52
Figure 5.7. Simulated and measured PAE versus input power at 220 MHz. 53
Figure 5.8. Simulation and measurement of gain versus input power at 220 MHz. 53
Figure 5.9. Simulation and measurement of maximum PAE frequency. 54

LIST OF TABLES

Table I: Performance Summary of The Previously Reported State of The Art……...…25

SYMBOLS AND ACRONYMS

VHF	Very High Frequency
ESA	Electrically Small Antenna
PA	Power Amplifier
SNR	Signal-to-noise Ratio
TVTL	Time-varying Transmission Line
PCB	Printed Circuit Broad
LNA	Low Noise Amplifier
TX	Transmitter
RX	Receiver
Q factor	Quality Factor
RF	Radio Frequency
SAW	Surface Acoustic Wave
CG	conversion gain
NF	Noise Figure

ACKNOWLEDGEMENTS

First, I am tremendously grateful for my advisor Prof. Yuanxun Ethan Wang for his patience with me and his guidance through this Ph.D. curriculum. His devotion, persistence, and drive have been a great source of strength when the research does not go well. I would also like to thank the electrical and computer engineering department at University of California Los Angeles for their help in transitioning from a doctoral student to doctoral candidate, to doctoral graduate.

I Also like to thank the support offered by my committee members at UCLA, Prof. Aydin Babakhani, Prof. Danijela Cabric, and Prof. Greg Pottie. I am aware of just how busy each faculty member is, so the time investments each made to sit on my committee, review his dissertation and listen to my presentations was much appreciated.

I also thank my labmates, who through endless hours of conversations have resulted in the superb results of this work

I would like to thank my family who have continued to support me through this whole of my life.

Finally, I thank my God for his grace and help in each step of my life.

VITA

Education

2017-2022 ***PhD candidate*** in **Electrical and Computer Engineering**
University of California, Los Angeles, USA

Selected Publications

[1] **Hedayati, M**., Yeung, L.K., Panahi, M., Zou, X. and Wang, Y.E., 2021. Parametric Downconverter for Mixer-First Receiver Front Ends. *IEEE Transactions on Microwave Theory and Techniques*, 69(5), pp.2712-2721.

[2] Santos, J.P.D., Fereidoony, F., **Hedayati, M**. and Wang, Y.E., 2020. High efficiency bandwidth VHF electrically small antennas through direct antenna modulation. *IEEE Transactions on Microwave Theory and Techniques*, 68(12), pp.5029-5041.

[3] Panahi, M.A., Yeung, L., **Hedayati, M**. and Wang, Y.E., 2022. Sub-6 GHz High FOM Liquid Crystal Phase Shifter for Phased Array Antenna. *IEEE Journal of Microwaves*, 2(2), pp.316-325.

Conference Presentations

[1] **Hedayati, M**., Diao, J. and Wang, Y.E., 2019, January. Adaptive communications with swarm aperture. In *2019 IEEE Radio and Wireless Symposium (RWS)* (pp. 1-3). IEEE.

[2] J.P. Santos, F. Fereidoony, **M. Hedayati**, and Y.E. Wang, "High Efficiency Bandwidth Electrically Small Antennas for Compact Wireless Communication Systems," 2019 IEEE MTT-S International Microwave Symposium (IMS), Boston, MA, 2019, pp. 1-4.

[3] **Hedayati, M**., Haung, Y. and Wang, Y.E., 2018, January. Code—modulated beamforming for mobile distributed array. In *2018 United States National Committee of URSI National Radio Science Meeting (USNC-URSI NRSM)* (pp. 1-2). IEEE.

Chapter 1

Parametric Amplification Background

1.1 Theory Of Parametric Amplifiers

Parametric amplification is a process of RF-RF power conversion that operates by pumping a nonlinear reactance with a large-signal RF pumping source to either produce mixing products with gain or to generate a negative resistance. Fundamentals of parametric amplification were well studied in the 1950s and 1960s that analyzed the power flow into and out of a nonlinear reactive element under excitation at its different harmonic frequencies. One of the most famous conclusions is Manley-Rowe relation that describes harmonics, intermodulation and how the energy transfer from one frequency to another frequency. Manley and Rowe began their analysis by considering a circuit shown in Fig. 1.1 that contains two voltage sources, V_1 and V_2, at frequencies f_1 and f_2, with their associated generator impedance, placed across a nonlinear capacitor. These two voltage sources are electrically isolated from one another through ideal bandpass filters. In addition to the two signal sources, an infinite array of resistive loads and bandpass filters have been connected across the nonlinear capacitor. These filters are tuned to the various sum and difference frequencies which will arise because of nonlinear reactance.

The Equations they obtained are

$$\sum_{m=0}^{\infty}\sum_{n=-\infty}^{\infty}\frac{mP_{n,m}}{mf_1+nf_2}=0 \qquad (1)$$

$$\sum_{n=0}^{\infty}\sum_{m=-\infty}^{\infty}\frac{nP_{n,m}}{mf_1+nf_2}=0 \tag{2}$$

These equations are remarkable as they are independent of the shape of the nonlinear reactance and the nature of the surrounding circuitry, assuming proper isolation of driving and harmonic currents. As a result, the Manley-Rowe relations provide a way to quantify the idealized metrics of parametric systems, such as gain and stability, and thus a figure of merit to evaluate the performance of circuit designs.

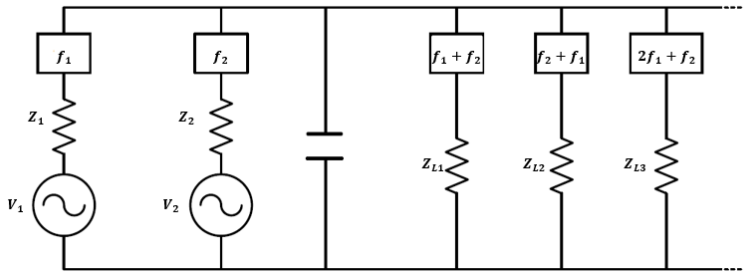

Figure 1.1: Circuit model for Manley and Rowe derivation.

1.2 A Linear Time-Varying Property of a Non-Linear Capacitance

The operation of a parametric mixer relies on the time-varying capacitance of a varactor device under a strong pump voltage. The pump is equivalent to the local oscillator in a conventional resistive mixer. As a matter of definition, the input to the parametric mixer is typically an RF input signal with the frequency of f_s and a pump signal with the frequency of f_p. The output can be at both the sum and difference frequencies between the input and the pump under the double sideband mixing case, or only at the difference frequency when the sum frequency is terminated reactively, which operates in single sideband mixing. For simplicity in this section, we consider the parametric mixing operates predominately under the condition of single sideband mixing,

where the output is called idler with a frequency of f_i. As the time-varying capacitance does not bear any loss theoretically, there is no power flow in or out of the circuit at frequencies other than the signal, idler, and pump frequencies. To analyze the time varying behavior of a nonlinear reactance, the circuit model shown in Fig 1.2 will be used. The shunt combination of C_0 (the mean value of the time-domain capacitance) and L_s in the input circuit is tuned at the signal frequency as input resonator, while in the output circuit, C_0 and L_i form output resonator tuned at idler frequency. G_L, G_i, and G_s represent output load, the resonator loss at idler, and the resonator loss at signal frequencies, respectively. The time-varying capacitance shown in Fig. 1.2 is realized by a varactor diode modulated by a pump source at $f_p = f_i + f_s$. Let the signal and LO pump voltages be as,

$$v_s = V_s \cos \omega_s t, \qquad v_p = V_p \cos \omega_p t \tag{3}$$

where $V_s \ll V_p$. The charge on the capacitor as a function of voltage v_p can be expanded in Taylor series. Considering only the first two terms,

$$q(v) \approx q(v_p) + \frac{dq(v_p)}{dv} v_s. \tag{4}$$

For convenience, the capacitance is thus defined by,

$$C(v_p) = \frac{dq(v_p)}{dv}. \tag{5}$$

The current through the capacitor is given by the time derivative of the charge.

$$i_t = \frac{dq}{dt} = \frac{d}{dt} q(v_p) + \frac{d}{dt} \left[C(v_p) V_s \cos \omega_s t \right]. \tag{6}$$

Since $C(v_p)$ is periodic with a fundamental frequency of ω_p, it can be expanded in a Fourier series.

$$C(v_p) = \sum_{n=0}^{\infty} C_n \cos(n\omega_p t). \tag{7}$$

$C(v_p)$ can be interpreted as a time-varying linear capacitance in this approximation, which yields the following time-varying form of (6),

$$i_t(t) = i_p(t) + \frac{d}{dt}[C(t)v_s(t)]. \tag{8}$$

Note that the first term in (8) is the current at the pump frequency and its harmonics, which does not interact with the input and output of parametric circuit directly. In the circuit, we are interested in determining the small signal voltage and current that are across and flow through $C(t)$ only at the signal and idler frequencies, which is described by the second term. As the higher order terms in (7) are at much higher frequencies than the interested frequency regime, truncating (7) to only the first two terms leads to a linear time-varying capacitance model as,

$$C(t) = C_0 + C_1 \cos(\omega_p t) = C_0 + 2\gamma C_0 \cos(\omega_p t) \tag{9}$$

where C_0, γ, and ω_p are the mean value of the time-domain capacitance, the capacitance modulation index defined by $C_1/2C_0$, and the pump frequency, respectively. To evaluate γ rigorously for a given pump voltage, one much follow (7) and perform Fourier expansions to calculate C_0 and C_1, which requires a full knowledge of the nonlinear capacitance behavior. For a quick and rough estimation, however, one could use the slope of the C-V curve, i.e., $\gamma \approx$

$\frac{C_{max}-C_{min}}{\frac{C_{max}+C_{min}}{2}}$, where C_{max} and C_{min} are the maximum and minimum capacitance value caused by the swing of the pump voltage.

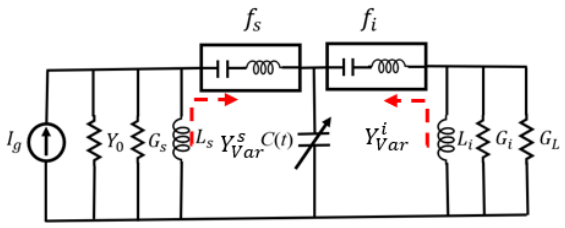

Figure 1.2: Simplified circuit model for parametric circuit.

1.3 Dissertation Outline

The thesis is summarized as follows. In Chapter 1, fundamentals of parametric amplification will be presented and in addition, Chapter 1 will develop the time variant concept for nonlinear capacitance.

In Chapter 2, mode analysis will be presented. This analysis is a good tool to predict the gain, efficiency and noise performance of a parametric circuit depend on termination of intermodulation tons and harmonics.

Chapter 3 utilizes the tools developed in Chapters 1 and 2 to design, a practical design of parametric downconverter which is supported by a comprehensive parametric conversion theory and circuit simulation results.

Chapter 4 a novel parametric matching technique for receivers with ESA is developed so that the receiver can achieve low noise performance over a broad bandwidth.

Chapter 5 presents a parametric power amplifier (PPA) with a unique load-modulation characteristic different from any existing architecture to enhance back-off efficiency. The proposed technique enables transmission of high peak-to-average-power ratio (PAPR) signals with high efficiency while maintaining excellent linearity.

Lastly, Chapter 6 a summary of the worked performed, as well as key contributions of the research, is included.

Chapter 2

Fundamentals Of Parametric Amplification and Mode Analysis

Parametric amplification is a process of RF-RF power conversion that operates by pumping a nonlinear reactance with a large-signal RF pumping source to either produce mixing products with gain or to generate a negative resistance. Fundamentals of parametric amplification were well studied in the 1950s and 1960s that analyzed the power flow into and out of a nonlinear reactive element under excitation at its different harmonic frequencies. One of the most famous conclusions is Manley-Rowe relation that describes harmonics, intermodulation and how the energy transfer from one frequency to another frequency. Based on Manley-Rowe relation the energy transferred among different intermodulation can be configured to have different characteristics depend on the termination of intermodulation tons and harmonics.

A. Double Sideband Upconverting Mode

In double sideband upconverting mode, a fixed frequency pump, at frequency f_p, mixes with an RF small signal source input, at frequency f_s, to produce two upconverted sidebands as shown in Fig. 2.1(a). Specifically, according to the Manley–Rowe relations, we can summarize the power flow in this circuit with

$$\frac{P_{p+s}}{P_p} = -\frac{\omega_{p+s}}{\omega_p} \tag{10}$$

$$\frac{P_{p-s}}{P_p} = -\frac{\omega_{p-s}}{\omega_p} \tag{11}$$

where P_{p+s} and P_{p-s} are the power flowing out to the IF port, and P_p is the power delivered to

by the LO. Therefore, the power from LO can be only injected two upper and lower sidebands while there is not any power exchange from signal to sidebands. Therefore, as (10) and (11) demonstrated, the low noise design can be obtained based on this double sideband operational mode.

B. Negative Resistance Mode

In the negative resistance parametric amplifier, currents are permitted to exist at the signal frequency ω_s, the pump frequency ω_p, and the idler frequency $\omega_i = \omega_p - \omega_s$ as shown in Fig. 2.1(b). we can summarize the power flow in this circuit with

$$\frac{P_{p-s}}{P_s} = \frac{\omega_{p-s}}{\omega_s} \tag{12}$$

where P_{p-s} is the power flowing out to the IF port, and P_s is the available power from RF signal. In this mode, current is permitted to exist at the idler frequency, further frequency mixing of power at the pump and idler frequencies occurs. This latter mixing causes harmonics of ω_p and $\omega_i = \omega_p - \omega_s$ to be generated; in particular, power at the frequency $\omega_s$is generated. When the power generated through frequency mixing exceeds that being supplied at the signal frequency ω_s, the diode appears to have a negative resistance. The transducer gain factor that comes from negative resistance at the input and output resonators can provide high gain for this mode.

C. **Single Sideband Upconverting Mode**

In the single sideband upconverting mode, a pump voltage at frequency ω_p and a signal at frequency ω_s are applied to the diode, and the output signal is taken at the higher frequency $\omega_p + \omega_s$ as shown in Fig. 2.1(c). we can summarize the power flow in this circuit with

$$\frac{P_{p+s}}{P_s} = -\frac{\omega_{p+s}}{\omega_s} \tag{13}$$

To achieve high gain with an up-converting mode requires a large ratio of output-to-input

frequency. In this mode, the power from both signal and pump frequency can be transferred to the idler. Therefore, this operational mode has highest energy efficiency characteristic.

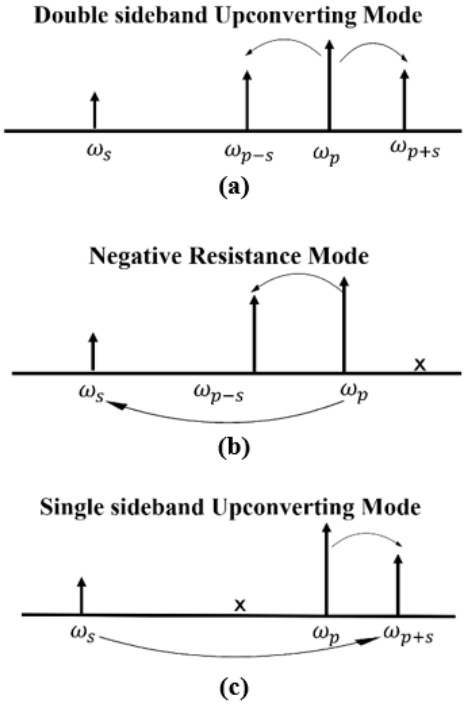

Figure 2.1: Three Parametric Amplification Modes – Lossless Cases. (a) Double sideband Upconverting Mode. (b) Negative Resistance Mode. (c) Single sideband Upconverting Mode.

Chapter 3

Parametric Downconverter for Mixer-First Receiver Front-Ends

3.1 Mixer-First Receiver Front-Ends Background

As the RF spectrum becomes increasingly crowded, demands on receiver flexibility and interference-tolerance are becoming more stringent. The increased traffic creates more in-band and out-of-band interferences, which may significantly degrade reception performance. Not only does the SNR of the receiver degrade under such interferences, the linearity of the LNA in the front-end may also suffer when strong blockers exist in the receiving band. Conventional receivers are equipped with multiple surface acoustic wave (SAW) filters for blocker attenuation. Although SAW filters can achieve excellent selectivity and very good linearity, they lack the programmability that is desired for software-defined radios.

To enable advanced radio concept such as cognitive radios, SAW-less receiver becomes a recent trend to study [1]-[3]. One of the more promising RF circuit topologies for such a front-end is the impedance translation technique (also known as an N-path filter) [4]-[7]. One of the transparency to achieve tunable receivers, where the bi-directionality of the RF mixer switches translate impedance on the mixer baseband port to its RF port, and vice-versa. However, the effectiveness of RF N-path filtering depends upon the performance of the multiphase clock, as there may be noise folding-back problems from the harmonic bands results from IQ phase mismatch [9]. With this technique, however, SAW filters cannot be eliminated completely because of odd harmonic image bands. Another SAW-less front end is presented in [10] which uses a low-noise amplifier (LNA) with an active feedback loop to achieve channel selectivity at

the input, but because of the LNA in the feedback loop, frequency compensation becomes complicated and sensitive to parasitic parameters.

Other promising RF circuit topologies for such a SAW-less front-end include mixer-first technique [11]-[13]. A current-mode passive mixer-first based receiver front-end with low mixer switch resistance and positive feedback is proposed in [11] to improve out-of-band interference handling. However, this mixer is lossy, and it increases the noise contribution of the next stages. Also, most of the literature on designed active mixers offer high conversion gain (CG) and linearity, but they suffer from poor noise performance that is likely to degrade the performance of the mixer-first receiver front-end. To overcome the noise problem of the above active and passive mixers, it is proposed here to develop a mixer-first receiver front-end based on parametric mixing. The parametric mixing and amplification effects were well-studied in the 1950s and 1960s to design parametric amplifiers [14]-[19]. However, with the emergence of the semiconductor transistors, the interests to use parametric effects in electronic applications gradually diminished. Recently, there has been a reemergence of interests in parametric mixing and amplification effects among microwave circuit designers to design low noise and highly linear components [20]-[26], which have operated either in a narrow band, de-generating modes or broadband traveling wave modes.

Parametric mixing leverages the parametric amplification approach that uses nonlinear/time-varying reactance for signal amplification or frequency conversion. Parametric mixing- based devices such as time-varying transmission line (TVTL) has been studied in [27] that shows low noise characteristics and broadband behavior. The basic system concept for mixer-first receiver

is illustrated in Fig. 3.1, where a parametric mixer such as TVTL is placed right after the antenna in place of the LNA.

The mixer converts the input signal frequency to the passband of a fixed filter placed after the mixer, while the blocker falls outside the passband and is suppressed. By changing the pump frequency, a different input frequency can be selected and converted to the passband of the filter. Historically, many considered that in order to obey Manley-Rowe relations [27], parametric frequency conversion can only achieve a positive conversion gain for frequency upconversion, i.e., when the output frequency is higher than the input frequency. Successful demonstrations of positive gain parametric conversion in the literature including [26] and [28]-[29] are almost all about frequency upconversion. Positive gain parametric downconversion has been discussed in [30] but no complete practical design and experimental results have been reported to our best knowledge. In this work, a practical design of parametric downconverter is proposed and supported by a comprehensive parametric conversion theory and circuit simulation results. It has also been experimentally demonstrated that the downconverting mixer is capable of achieving a positive conversion gain and mitigating the noise figure issue of active mixers or the conversion loss issue of passive mixers. The proposed technique utilizes the negative resistance in a resonator created by parametric pumping, which offers power gain to compensate not only loss introduced by its passive components with a finite quality factor, e.g. capacitors, inductors/microstrips but also the gain reduction caused by frequency down-conversion.

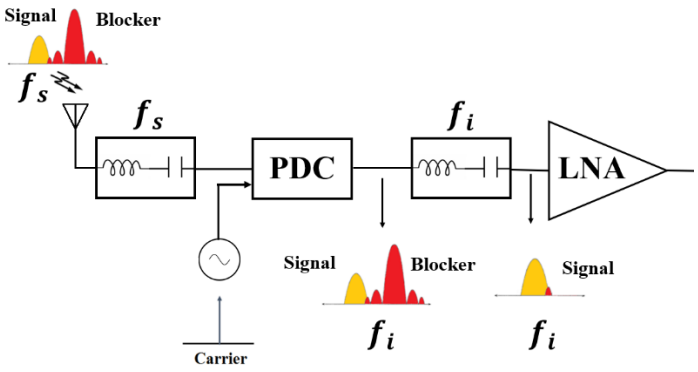

Figure 3.1: Mixer-first receiver architecture.

3.2 Theory

The operation of a parametric mixer relies on the time-varying capacitance of a varactor device under a strong pump voltage. The pump is equivalent to the local oscillator in a conventional resistive mixer. To compute the operating characteristics of the parametric frequency converter, the circuit model shown in Fig 1.2 will be used. The nonlinear capacitor is modeled as a linear time-variant capacitor using small-signal approximations as indicated in (9). It is thus convenient to evaluate the second term in (9) as a function of the voltage, obtaining an equivalent linearized admittance matrix defined across these two different frequencies. For any given pump voltage, the input and output behavior of the pumped nonlinear capacitor can thus be modeled by a small-signal admittance matrix defined across the different frequencies [31]. To construct this matrix, we will deal with real quantities in complex form. For example, the capacitance variation will be expressed as,

$$C(t) = C_0\left(1 + 2\gamma\cos\left(\omega_p t\right)\right) = C_0 + C_0\gamma\left[e^{j\omega_p t} + e^{-j\omega_p t}\right]. \quad (14)$$

Similarly, the small-signal voltages and currents at frequencies ω_s and $\omega_i$will be expressed as,

$$\begin{cases} v = V_s e^{j\omega_s t} + V_s^* e^{-j\omega_s t} + V_i e^{j\omega_i t} + V_i^* e^{-j\omega_i t} \\ i = I_s e^{j\omega_s t} + I_s^* e^{-j\omega_s t} + I_i e^{j\omega_i t} + I_i^* e^{-j\omega_i t} \end{cases} \tag{15}$$

The coefficients V_s, V_i, I_s and I_i are complex quantities containing phase information. The overall expressions for v and i at any given frequency, however, are real since they consist of the sum of a quantity and its complex conjugate. They are related to each other through,

$$i = \frac{d}{dt}[C(t)v(t)]\,. \tag{16}$$

Therefore, the resulting equations by expanding (16) at the different frequencies yield the following matrix form,

$$\begin{pmatrix} I_s \\ I_i^* \end{pmatrix} = \begin{pmatrix} j\omega_s C_0 & j\omega_s \gamma C_0 \\ -j\omega_i \gamma C_0 & -j\omega_i C_0 \end{pmatrix} \begin{pmatrix} V_s \\ V_i^* \end{pmatrix} \tag{17}$$

where the coefficients I_s, I_i, V_s, V_i are complex current and voltage quantities containing phase information defined at the signal and idler frequencies respectively. ω_s and ω_i represent signal and idler angular frequencies. By eliminating I_i and V_i the equivalent admittance of the nonlinear capacitor at the signal frequency can then be derived [see appendix A] as,

$$Y_{Var}^{s} = j\omega_s C_0 - \frac{\omega_s \omega_i \gamma^2 C_0^2}{Y_i^* - j\omega_i C_0} \tag{18}$$

where Y_i $(= G_i + G_L + \frac{1}{j\omega_i L_i})$ and Y_s $(= G_s + Y_0 + \frac{1}{j\omega_s L_s})$ are the admittance seen by the nonlinear capacitor at idler and signal frequencies, respectively. In a similar approach, the equivalent admittance of the nonlinear capacitor at idler frequency can be derived as,

$$Y_{Var}^{i} = j\omega_i C_0 - \frac{\omega_s \omega_i \gamma^2 C_0^2}{Y_s^* - j\omega_s C_0}. \tag{19}$$

The second terms in (18) and (19) are equivalent to a negative conductance when Y^*_i and Y^*_s are resonant with C_0 at idler or signal frequencies. In other words, the nonlinear capacitor in the small-signal model at resonance frequency can be modeled by linear capacitor C_0 in parallel with a negative conductance of $G_{Var}^{i} = -\frac{\omega_s \omega_i \gamma^2 C_0^2}{G_s + Y_0}$ or $G_{Var}^{S} = -\frac{\omega_s \omega_i \gamma^2 C_0^2}{G_i + G_L}$. Therefore, the circuit can operate in negative resistance/conductance mode with an arbitrarily large gain; in fact, oscillation can occur when the magnitude of negative conductance is greater than the source or load conductance. We will show in the rest of this part when the circuit operates below the oscillation threshold, such a circuit behaves as an amplifier and a frequency converter at the same time.

For the two-port configuration of the proposed resonator as shown in Fig. 1.2, its available power gain can be expressed as [see appendix A],

$$G_a = \frac{\omega_i}{\omega_s} \cdot \frac{4\gamma^2 Q_s Q_i}{(1 - \gamma^2 Q_s Q_i)^2} \tag{20}$$

where Q_s and Q_i are loaded quality factor of signal and idler loop, respectively. By considering only the noise added by the loss of the input and output resonators (G_s and G_i) at the signal and idler frequencies, the noise figure expression can also be derived as,

$$F_N = \left(1 + \frac{G_s}{Y_0}\right)\left(1 + \frac{\omega_s}{\omega_i}\frac{1}{\gamma^2 Q_s Q_{iu}}\right) \tag{21}$$

where Q_{iu} is the unloaded quality factor of the idler loop. The fractional bandwidth of the downconverter is,

$$b = \frac{1}{Q_s}(1 - \gamma^2 Q_i Q_s) \tag{22}$$

which states that the fractional bandwidth is limited by the bandwidth of the input circuit. Derivations for these expressions are given in the Appendix. Notice that a few insights can be obtained from (20) and (21). Firstly, in (20), the first term ($\frac{\omega_i}{\omega_s}$) is the gain reduction due to the frequency down-conversion and the second term is a transducer gain factor that comes from negative resistance at the input and output resonators that can provide an overall gain of the circuit. Also, it should be noted that (20) has a negative sign in the denominator that leads to the possibility of oscillation. But by proper selection of Q_s and Q_i, the circuit can operate below the oscillation threshold. Secondly, the noise figure in (21) not only depends on the resonator loss at signal frequency but also on the pumping power. It should be noticed the capacitance modulation index (γ) reflects the effect of LO power. Indeed, γ is the ratio of the amplitude of the capacitance variation due to the LO signal to the mean capacitance of varactor. Therefore, the larger the pumping power, the lower the noise figure. Based on equation (20) and (21), Fig. 3.2 illustrates the down-converter gain and noise figure for different values of input quality factor when f_s=1.9GHz, f_p=3.35GHz, Q_i=2.48, Q_{iu}=27.3, γ=0.21, $G_s \ll Y_0$ and $G_i \ll G_l$. As depicted, the noise figure and mixer gain can be controlled by the input quality factor. As an example, the noise figure is around 2.8 dB with 10 dB gain when Q_s=5. The dependency of gain and noise figure to the modulation index is also plotted in Fig. 3.3. Also, to validate the gain and noise figure expressions (20) and (21), a parametric mixer circuit schematic is setup in ADS with a bridge connection of four varactor diodes. The balanced configuration provides isolation between the pump circuitry and the signal/idler circuitry so that it emulates the ideal schematic of parametric mixer with time-varying capacitors illustrated in Fig.1.2. The ADS harmonic

balance (HB) simulation results for conversion gain and noise figure under different quality factors and capacitance modulation indexes are also added to Fig. 3.2 and Fig. 3.3 that show acceptable agreement with analytical results. The capacitor in equation (9) approximates the real capacitor in equation (7) which makes some differences between simulation and analytical results. In the analytical simulation, it is observed that high gain and low noise design can be achieved by increasing the capacitance modulation index. However, there is an upper bound for γ to avoid instability region that we will discuss in the next section.

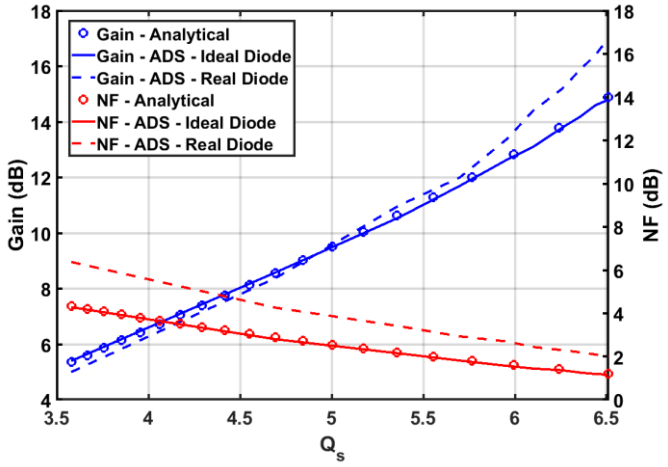

Figure 3.2: Mixer gain and noise figure versus input quality factor.

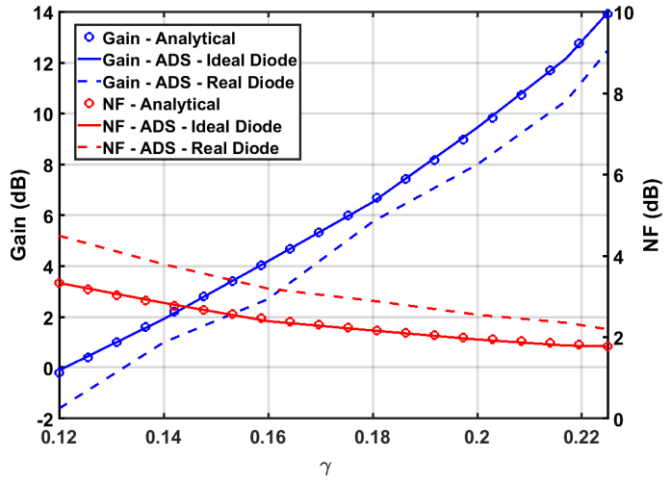

Figure 3.3: Mixer gain and noise figure versus capacitance modulation index.

3.3 Stability Condition

It is well known that negative resistance can make oscillation in the circuit; in fact, a device is used to supply an amount of energy equal to the energy dissipated, the circuit can sustain oscillations. In terms of signal frequency, the equivalent circuit shown in Fig. 1.2 can be redrawn as the one shown in Fig. 3.4 and the stability condition can be derived according to this circuit. Stability condition for this circuit thus becomes,

$$G_{var}^{i} < Y_0 + G_s \tag{23}$$

which can be further written as,

$$f_i \gamma^2 Q_s^2 < f_s \tag{24}$$

where $Q_s = \frac{\omega_s C_0}{Y_0 + G_s}$.

In a similar approach for idler frequency, we can write,

$$G_{var}^{s} < G_l + G_i \tag{25}$$

which can be further written as,

$$f_s \gamma^2 Q_i^2 < f_i \tag{26}$$

where $Q_i = \frac{\omega_i C_0}{G_i + G_l}$.

By considering the bi-lateral conditions defined by (24) and (26) at the same time, we can obtain the stability condition for the circuit as,

$$Q_s Q_i < \frac{1}{\gamma^2}. \tag{27}$$

Fig. 3.5 shows the stability region for downconverter for two different conditions when f_s=1.9GHz, f_p=3.35GHz, and γ=0.215. As can be seen in both cases, when Q_s is close to $\frac{1}{Q_i\gamma^2}$, the circuit starts to oscillate.

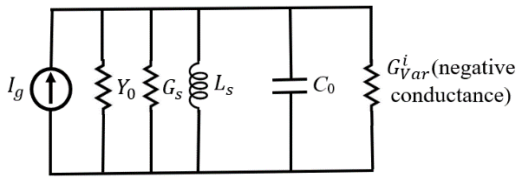

Figure 3.4: Equivalent circuit at signal frequency.

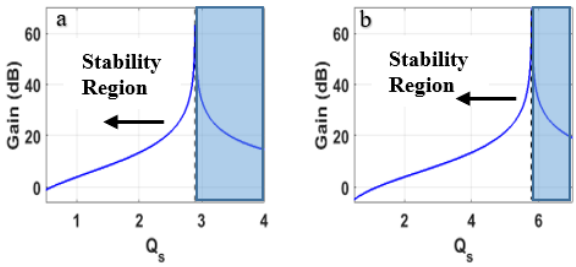

Figure 3.5: Stability region for downconverter. (a) Q_i=6, (b) Q_i=3.

3.4 Design Considerations

The schematic and PCB layout of the proposed parametric down-converter are shown in Figs. 3.6(a) and 3.6(b). The microstrip line of impedance Z_2 and the varactor-loaded microstrip line of impedance Z_1 are key components of this converter. Ideally, both Z_2-line and varactor-loaded Z_1-

line are quarter-wave long at the signal frequency. Mathematically, the lengths of these two lines can be determined by,

$$\theta_2(\omega_s) = \frac{\pi}{2}, \tag{28}$$

$$\theta_1(\omega_s) = \tan^{-1}\left(\frac{2}{\omega_s C_0 Z_1}\right) \tag{29}$$

providing that C_0, Z_1, and Z_2 are properly chosen (i.e. depending on substrate properties, PCB manufacturing tolerances, and varactor characteristics).

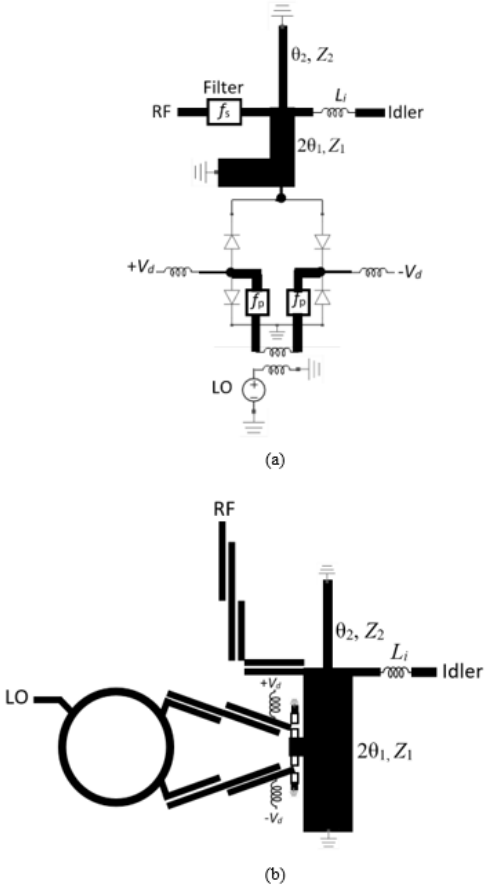

Figure 3.6: Microstrip parametric down-converter mixer (a) Schematic. (b) Layout.

The parameters obtained for a downconverter operating at the signal frequency of 1.9 GHz are Z_1 = 14 Ω, Z_2 = 70.1 Ω, θ_1 = 56º, θ_2 = 90º, C_0 = 8 pF. The impedance looking at the point where these two lines connected should theoretically be open-circuited. In other words, these lines together act as a parallel resonator at the signal frequency as depicted in Fig. 3.7(a). Notice, however, that the idler portion of the circuit will introduce some loading effects and they should be taken into consideration.

At the idler frequency, since it is lower than the signal frequency, the impedance at the connection point will be inductive. For this reason, two transmission lines linked by a series inductor is used to bring (i.e. rotating clockwise on the Smith chart) the overall layout resonating (open-circuited) at the idler frequency. In other words, it acts as a parallel resonator when looking into the idler port as depicted in Fig. 3.7(b). Similarly, the loading effects due to the signal portion of the circuit should be taken into consideration. The main purpose of the inductor L_i is to block out the RF signal coming out from the idler port. It should be noted that the single time-varying capacitor shown in Fig. 1.2 is replaced by a diode bridge for differential pumping of the resonator and a strong isolation of the pumping source from the signal and the idler. The differential feed is a balun as well as a bandpass filter to reject all frequencies except the pump frequency, which is 3.35 GHz in this case. The filter at the RF input is not necessary for the operation of the proposed circuit as the input resonator has already acted as an open circuit for signal frequency and a short circuit for idler frequency. It is used to maximize the isolation between RF and idler for the sake of S-parameter measurements so that the vector network analyzer does not suffer power imbalance. In general, high Q passives are preferred for the performance of the parametric amplifier on-chip. For example, in [32], high Q (Q>30) on-chip inductors such as planar helical inductors have been developed on GaAs chips and applied in

parametric circuits. It is worth mentioning that the values of C0 and ɣ are chosen based on the data sheet of the commercially available varactor diode from Skyworks Co., Ltd. The voltage dependent capacitance behavior of the varactor is shown in Fig. 3.8. The capacitance versus voltage relation appears to be approximately linear for biasing voltage from 0 to -3V.

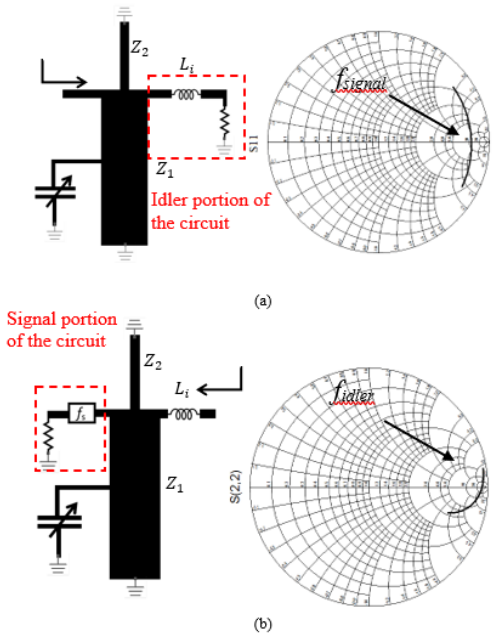

Figure 3.7: Input and output resonators (a) Single-port signal resonator. (b) Single-port idler resonator.

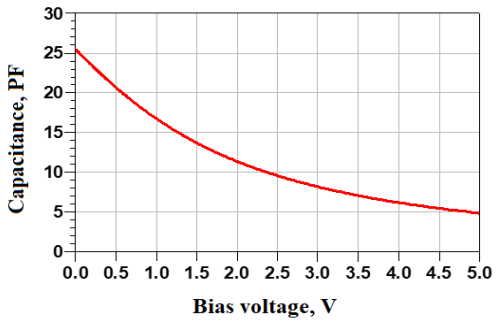

Figure 3.8: Capacitance-versus-voltage behavior of the varactor diode.

3.5 Measurement Results

To prove the proposed concept, the mixer is designed and fabricated on a Rogers board which is shown in Fig. 3.9. In the experiment, all varactors are reversely biased with 3 V dc voltage a mean capacitance of 8 pF. One inductor with a value of 15 nH is used between signal and DC ports to isolate RF-DC path. In this setting, the RF and LO frequency is set to 1.9 GHz and 3.35 GHz with an RF power of −20 dBm and LO power of 27dBm corresponding to a modulation index of approximately γ=0.31. A Keysight N5241A PNA-X is used for S parameter and noise figure measurements.

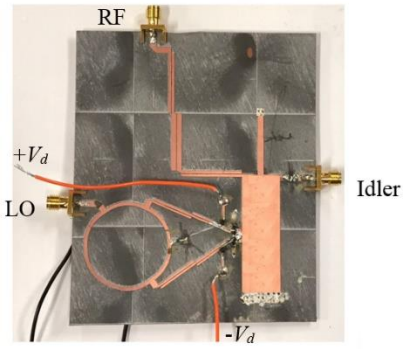

Figure 3.9: Fabricated microstrip parametric down-conversion mixer.

The simulated and measured gain and noise figure characteristics are shown in Fig. 3.10. The measured maximum gain is about 10 dB at 1.45 GHz with 37 MHz gain bandwidth. The minimum and maximum noise figure is 3.8 dB at 1.438 GHz and 2.8 dB at 1.46GHz, respectively. There are two external narrow-band filters at LO and Idler ports in the measurement which makes some disagreement outside the operation bandwidth for simulation and measurement results for noise figure.

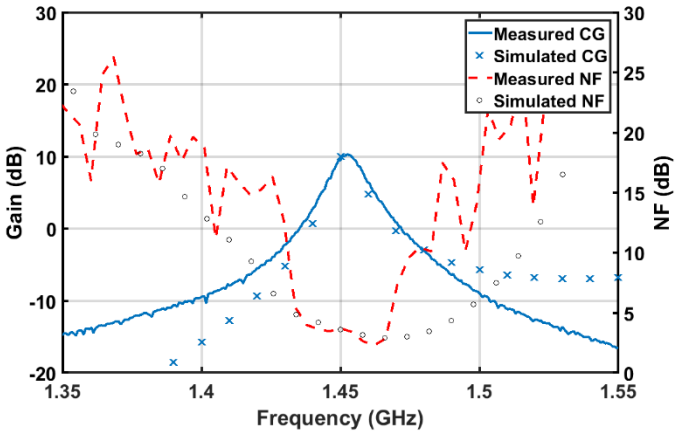

Figure 3.10: Measured and simulated gain and noise figure of the fabricated parametric mixer.

Fig. 3.11 shows the measured 1-dB compression point. In this setting, the output IF is set to 1.45 GHz with an RF frequency of 1.9 GHz whose power is swept from −25 to 10 dBm. The measured input 1-dB compression point is about +7 dBm (16dBm output P1dB) with +16 dBm IIP3. In table I, the performance of the proposed mixer is summarized and compared with other low noise mixers [33]–[38] as well as a couple of commercial off the shelf product specs. From this table, the proposed architecture achieves the best NF and linearity amongst previously published state-of-the-art designs while it provides a reasonable positive gain. The LO power consumption of the device is in the higher end, however, due to the limited quality factor of the varactor diodes. As the proposed mixer specifically emphasizes low noise and high linearity applications, it is difficult to apply a comprehensive figure of merit for comparison to other designs that are mainly targeted at low power applications. It should also be noted that linearity specs reported in table I from many existing works are obtained with linearization techniques while no linearization or IM3 cancellation technique has been applied for the proposed work.

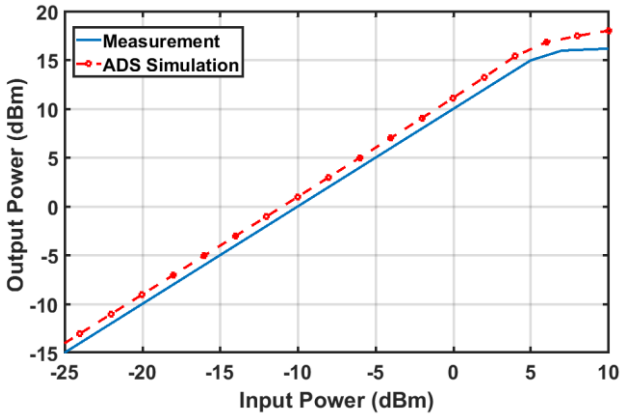

Figure 3.11: Measured and simulated output versus input power.

TABLE I
PERFORMANCE SUMMARY OF THE PREVIOUSLY REPORTED STATE OF THE ART

Mixer	*MDA4-752H+	**334LP4E	[33]	[34]	[35]	[36]	[37]	[38]	This work
Technology	InGap HBT	SiGe	CMOS 65 nm	CMOS 0.18-μm	CMOS 0.13-μm	CMOS 0.13-µm	CMOS 110-nm	CMOS 0.13-µm	Parametric
RF Center Frequency (GHz)	3.85	1.65	3.5	1.9	3.25	2.28	2.4	3.1	1.9
CG (dB)	7.6	-1	18	24	17.5	13.5	19	15	10
DSB NF (dB)	8.6	8	5	9.5	3.9	4.6	5.1	4.2	3.3
IIP3 (dBm)	16	26	-3	7	0.84	-11.5	-7	2.5	16
DC Power (mW)	705	865	16	10	34.5	16.8	3	25.5	0
LO Power (dBm)	0	0	14.5	-	0	-	-1	-2	27

*Mini-Circuits, MDA4-752H+.
** Analog device, HMC334LP4 / 334LP4E.

Chapter 4

Matching of Electrically Small Antennas for broadband, Low Noise Reception

4.1 Electrically Small Antenna Matching Background

The very-high-frequency and ultrahigh-frequency bands are used in many communications systems, in part due to its unique low loss long-distance propagation characteristics [39]. However, due to the long wavelengths of the electromagnetic (EM) waves at these frequencies, practically antenna size at those frequencies is considered electrically small. The rapid advances in mobile communication systems have led to increasing demands on higher data rates and it encourages the use of broadband antennas in communication systems. However, alongside Wheeler and Chu's findings about lower bound for the quality factor of an antenna with a given electrical size [40], [41], the Bode-Fano bound limit [42] the realized gain of ESAs needs to be traded for broader BW. Chu's limit shows antenna radiation Q-factor, Q_{rad}, is inversely proportional to electric size of the small antenna. This relationship indicates how fast energy delivery efficiency and bandwidth product of a small antenna decrease by miniaturization. To overcome these fundamental limits, a significant amount of efforts have been made since 1950s using multimode and/or non-LTI techniques [43]–[45] which almost all of them, have been implemented for transmit antennas., non-Foster and active impedance matching networks for ESAs [46]–[49].

In recent years, Non-Foster impedance matching networks (NICs) is proposed can overcome the gain-bandwidth limitations of passive small antennas. However, for an NFC matched antenna in

the receiving mode, the noise added by the active NFC can degrade the received signal-to-noise ratio (SNR) beyond an acceptable limit and counteract the benefits of bandwidth improvement.

Due to design of low noise microwave components, parametric devices as nonlinear and/or time-variant components have recently regained the attention of researchers [20], [32], [50-51]. Recently, integrating parametric amplifiers into antennas have also been attempted in [52-54], however, the amplification is still resonance based which operate only over a narrow band. In this paper, we propose a concept analogous to a recent work utilizing parametric amplification of nonlinear electron spin precessions in ferrite to [55] allow detection of extremely weak magnetic field with a small form factor sensor over a very broad band with almost no frequency dependence. Leveraging on the advanced electronics and IC technology, the proposed approach can indeed achieve the desired broadband low noise performance at HF, VHF or even UHF bands.

4.2 Motivation Of Matching Based on Parametric Amplification

Traditionally the antenna matching to the receiver is carried out as two separate tasks. A common interface impedance, e.g., 50Ohm, is often set at first so that the antenna output is conjugately matched to this common impedance through a matching network. On the other hand, the input of a low noise amplifier (LNA) as the first stage of the receiver is also designed to match to this common impedance, although the matching may not be exactly conjugate as oftentimes a minimum noise figure of the LNA is yielded at a condition slightly off from the conjugate match at the input. This strategy guarantees the best signal to noise ratio (SNR) of the receiver system if the signal is within the matched bandwidth and when loss does not present in

the matching network as the maximum amount of signal power is delivered to the LNA and consequently the impact of the noise added by the LNA can be minimized.

For ESAs, their radiation resistances are often very small, and with sub-Ohm values. In addition to their high radiation Q, transforming the extremely low radiation resistances of the ESAs to 50Ohm will inevitably incur great loss and narrow bandwidth in the impedance matching network. Same may be applied for the impedance transformation network between the LNA and the common impedance interface, particularly when low quality factor inductors are used as part of the matching network. The loss in the matching network will elevate the noise level in the receiver and reduce its sensitivity. The SNR benefit of maximize the signal power delivered to the LNA may no longer be obtained. It has thus been shown [56] that ESAs directly connected to a LNA without going through conjugate impedance match may exhibit a better SNR in the receiver, especially over wide operating bandwidth.

On the other hand, to achieve the desired SNR or sensitivity performance of the receiver, conjugate match may not be needed at all if the first stage of the receiver is close to noiseless and with positive gain. When the thermal noise of the environment is dominant in antenna, a lossless mismatch of the antenna to the LNA reduces the delivered signal power to the LNA as well as the noise power. For example, specialized field sensors such as SQUID or SERF have been used to detect extremely weak low frequency magnetic field over a broad bandwidth, much superior to what a conventional antenna can offer, as it is no longer necessary to maximize the signal power delivered to combat the noise added by the sensor. Recently, a solid-state magnetic field sensing technique called RF precession modulation technique is also proposed [55]. With such sensors, very weak magnetic field can be detected with a small form factor sensor as the field to

be detected modulates the electron spin precession at resonance and is parametrically amplified by the material before it is finally detected by the inductive coil.

In this effort, we develop a novel parametric matching technique for receivers with ESA so that the receiver can achieve low noise performance over a broad bandwidth. We propose to match an electrically small dipole or bowtie antenna directly to a parametric amplifier, without using any inductors as they are often of low-quality factors and their loss contribute additional noise to the receiver. The parametric amplifier operates in a time-varying fashion, driven by a higher RF frequency pump. It exhibits a high impedance, time-varying capacitive load to the ESA. Therefore, the low frequency voltage output from the ESA is detected at the input of the parametric amplifier, being amplified and upconverted to the proximity of the pump frequency at the output with minimum contamination of noise in this process.

4.3 ESA Matching with Parametric Amplifier Design

Parametric amplifiers are based on nonlinear reactive devices such as varactor diodes. The exhibit time-varying reactance under the excitation of a high frequency pump so that the incoming signal at a lower frequency is amplified or upconverted with a positive gain.

Analogous to [55], we propose to develop a parametric amplifier with a balanced varactor diode bridge with double sideband idler outputs to have the best noise performance [See Chapter 2]. The structure is shown in Fig. 4.1 where the signal V_s is incident on the top and bottom of the diode bridge while the pump is added from the left and the right ends of the bridge. The electrically small bowtie is directly connected to the diode bridge, without going through any impedance matching or transformation circuit. The idler signals V_i are extracted at the pump port and can be separated from the pump by using a circulator or a diplexer. Comparing to other

existing works [52-54] that use resonant matching network and diplexers to separate the different tones (signal, idler and pump), the balanced diode bridge allows the signal path to be isolated from the pump and idler paths so that the ESA only sees the diode capacitance. This is critical to the noise performance of the receiver as any matching inductors or filters at the signal path may add additional noise to the system. The pump frequency is selected to be sufficiently high comparing to the signal so that the two idler sidebands are falling within the bandwidth of the resonance of the pump loop.

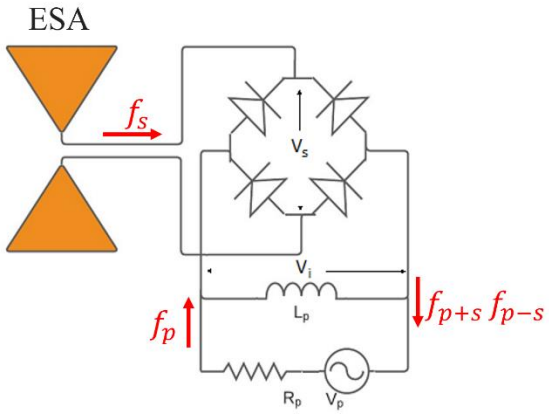

Figure 4.1. Parametric matching concept.

Matching inductors and impedance transformation circuits can be added at the pump and idler port to assure a high energy delivery efficiency and the impact of these circuits to the noise performance is minimum as the signal is already amplified at the idler outputs. The double sideband idler parametric amplifier offers better gain than the parametric up-converter and better noise comparing to the negative impedance parametric amplifier [57].

To establish the standard of quantifying the noise performance of the receiver with ESA (Fig. 4.1), we propose to use the Chu's ESA broadband equivalent circuit model [40] for the lowest

order electric dipole (TM_1) which were intended to represent the near field energy characteristics of both modes outside a sphere of radius a that encloses the antenna that it is shown in Fig 4.2. In this study, we calculate the noise figure of the system with ESA included, assuming the radiation resistance in Chu's model is the source resistance for noise figure calculation. Based on this strategy, the maximized transducer gain at optimum matching condition ($C_a = C_0$) can be expressed as [see the Appendix B]

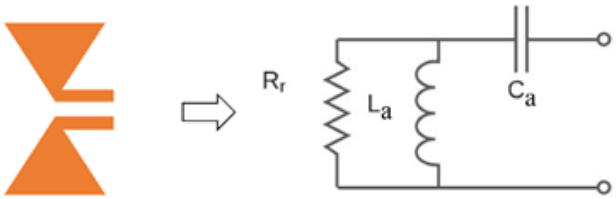

Figure 4.2. Electrically small dipole represented by an equivalent circuit model for TM_1 mode.

$$G_{T,max} = \frac{1}{2}\frac{Q_d}{Q_a}\gamma^2 \tag{30}$$

where Q_a and Q_d are the radiation quality factor of the antenna and the intrinsic quality factor of the varactor diode at the original signal frequency, respectively. γ is the capacitance modulation index defined by $C_1/2C_0$, C_0 is the mean value of the time-domain capacitance, and C_1 is the time variant capacitance. By considering only the noise added by the loss of the input and output resonators at the signal and idler frequencies, the NF expression Under the maximum gain condition can also be derived as

$$F_N = 1 + \frac{Q_a}{Q_d}\left(1 + \frac{2}{\gamma^2}\right) \tag{31}$$

Since γ has a maximum value of 0.5, it is evident from (30) and (31) that the diode quality factor needs to be at least one order of magnitude higher than the radiation quality factor of the ESA in order to realize positive gain and low noise figure (NF<3dB).

To prove of the above theory, an electrically small planar bowtie dipole is designed with a maximum dimension of 1.15m, which corresponds to *ka=1/2* at 64MHz. The antenna is simulated in the Keysight ADS Momentum, and its input impedance is used to fit to a Chu's TM_1 mode circuit model. This yielded the component values of R_r=490Ω, L_a=183nH and C_a=9pF. The GaAs varactor diodes are used from GCS's 1um InGaAs HBT process. The capacitance modulation index γ is approximately 0.3 and its cutoff frequency is approximately 140GHz. At 30MHz, the diode Q is 2580 and the radiation Q of the electrically small bowtie dipole with a dimension of ka=1/2.6 at 50MHz is approximately 85. The input frequency is from 30MHz to 100MHz, and the parametric amplifier is pumped at 2.5GHz with a power of 26dBm, which upconverts the input to 2.45 to 2.49GHz for the lower sideband and 2.51 to 2.55GHz for the upper sideband. Multiple varactor diode bridges from the GCS's 1um InGaAs HBT D5 process are placed in parallel to yield a 9pF mean capacitance. The upconverted idler signals at around 2.5GHz are amplified and then downconverted with the same pump to avoid contamination of the LO phase noise. The simulation setup is shown in Fig 4.3. The simulated gain of the entire system, excluding the gain of the idler amplifier is plotted in Fig.4.4(a) and the simulated noise figure is plotted in Fig.4.4(b), compared against the analytical results given by (30) and (31). The comparison between the theory and the circuit simulations agree very well in both gain and noise figure predictions and the slight deviation in gain for higher frequency is due to the bandpass behavior of the pump/idler port. Circuit simulations show that a positive transducer gain and a noise figure lower than 3dB are achieved with the parametric matching approach when the input

frequency is greater than 45MHz. To validate the performance of the proposed matching network, we will need to define the effective efficiency of the time-varying antenna. A lossy antenna delivering its received power to a matched resistive load will have a noise figure of 1/η, where η is its radiation efficiency. Therefore, the effective efficiency of the antenna with parametric amplifier can be defined as the inverse of its noise figure. We define the lower bound of the useful frequency band is governed by the noise figure requirement, e.g., 3dB noise figure or 50% effective efficiency. The upper bound of the frequency band is defined by the ka<1/2 requirement. In the current parametric matching design presented in Fig.4.3, the useful frequency band is from 45MHz to 64MHz. We thus derived the efficiency bandwidth product metrics assuming a center frequency of 54.5MHz. The electrically small bowtie dipole has a radiation Q of 85 at 54.5MHz, with ka=1/2.6, an effective efficiency of 60% and a fractional bandwidth of 37%. The simulation shows parametric matching network can have an effective efficiency bandwidth product that is 8 times of Chu's limit and 36 times of that is defined by the actual radiation Q of the antenna.

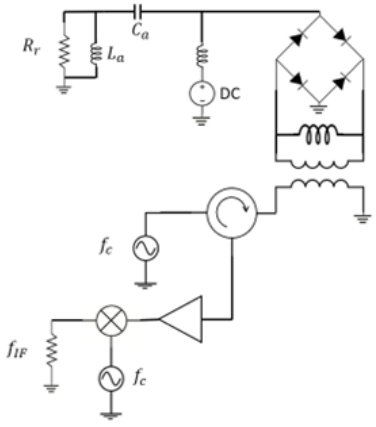

Figure 4.3. Simulation schematic of the matching circuit with the parametric amplifier designed for the electrically small antenna.

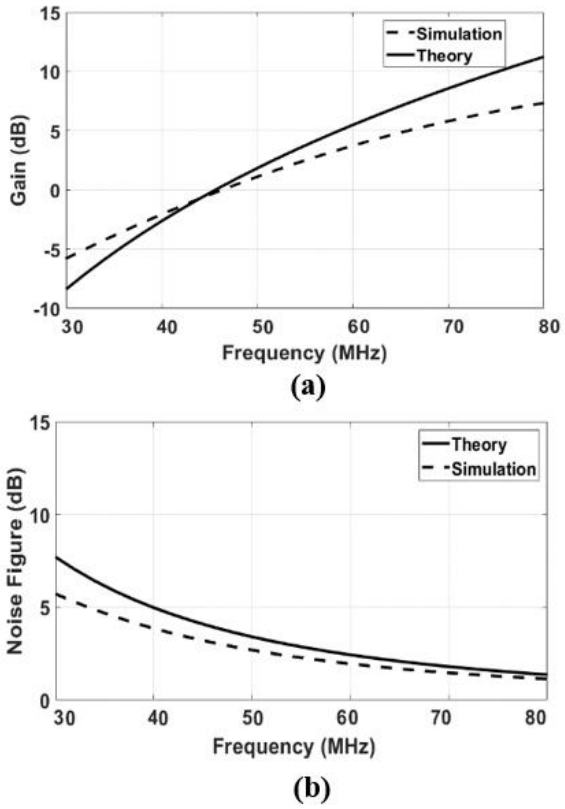

Figure 4.4. Simulated results of the parametric matching technique comparing to the theoretical prediction (a) gain (b) noise figure.

4.4 Experimental Characterization of The Parametric Matching

A. Circuit Design

The radiating part of the proposed parametric amplifier is an electrically small planar bowtie dipole with a maximum dimension of 0.12λ at 50 MHz. We specifically designed the antenna with electrically small dimensions to have high quality factor (Q_{rad}) at 50 MHz . The bowtie dipole was constructed from copper tape. The antenna was simulated in the Keysight ADS Momentum and its input impedance is used to fit to a Chu's TM_1 mode circuit model which yielded the capacitance values C_0=9pF. The simulation results also show that the intrinsic quality

factor of the antenna is high (Q_{rad}=85) at 50 MHz, due to its large reactance and low radiation resistance. It is evident from (30) and (31) that the diode quality factor needs to be higher than the radiation quality factor of the ESA in order to realize positive gain and low noise figure under optimum matching condition ($C_a = C_0$). Therefore, we used GaAs Hyperabrupt varactor diodes from MACOM (MA46H071). The voltage-dependent capacitance behavior of the varactor is shown in Fig. 4.5. The capacitance modulation index γ is approximately 0.36 and its cutoff frequency is approximately 300GHz. At 50MHz, the diode Q is 4500. Multiple MA46H071varactor diode bridges are placed in parallel to yield a 9pF mean capacitance to satisfy optimum matching condition it is shown in Fig. 4.6.(a). To satisfy a high energy delivery efficiency, matching inductors and impedance transformation are added in LO port as shown in Fig. 4.6(b). Fig. 4.7 shows the results of the measured return loss from pump port at 2.6 GHz. The pump frequency is selected to be sufficiently high comparing to the signal so that the two idler sidebands are falling within the bandwidth of the resonance of the pump circuit. The impact of pump circuits to the noise performance is minimum as the signal is already amplified at the idler outputs. The electrically small bowtie is directly connected to the diode bridge, without going through any impedance matching or transformation circuit a shown in Fig. 4.6(c).

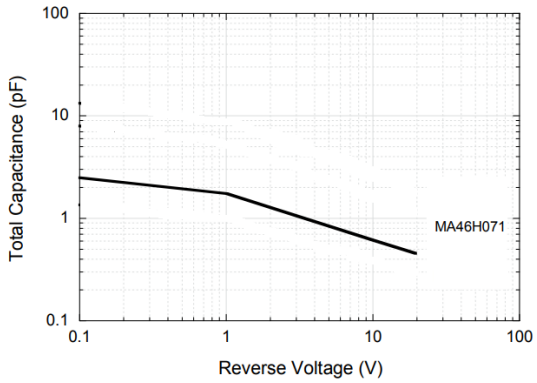

Figure 4.5. Simulated results of the parametric matching technique comparing to the theoretical prediction (a) gain (b) noise figure.

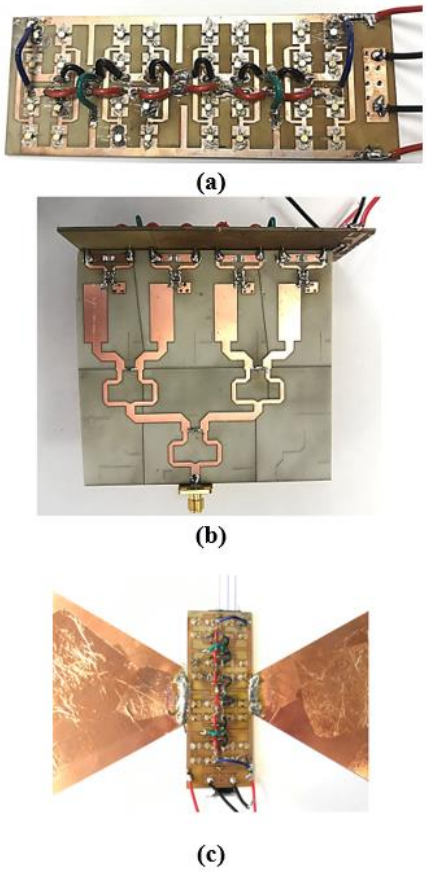

Figure 4.6. Parametric matching circuit design. (a) Multiple parallel bridge diode. (b) LO matching. (c) Interconnection between antenna and diode bridges.

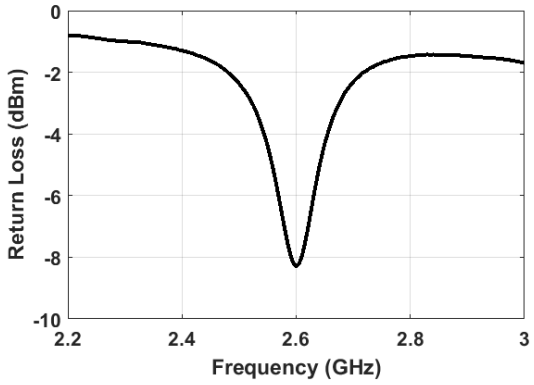

Figure 4.7. Return loss from pump port.

B. Measurement Setup

The proposed matching system has been prototyped at the UCLA Digital Microwave Laboratory. A measurement set up, as presented in Figure 4.8(a), was implemented to evaluate the antenna performance. In this setup, a small loop antenna was connected to the Tektronix signal generator and a power amplifier to form a transmit system. The prototyped structure was configured as a Rx antenna, and an R&S spectrum analyzer measured its output power spectrum. The LNA before spectrum analyzer is used to be sure the dominant noise is antenna noise. The distance between the Tx and Rx antennas was about 10m. In the experiment, all varactors are reversely biased with a 4V dc voltage and a mean capacitance of 1.1 pF. A signal generator was connected to the circuit as pump source. The pump-source frequency, f_p, was set to 2.6 GHz with a power of 34dBm while the Tx frequency, f_s, swept from 45 MHz to 64 MHz. For comparison, a reference setup is implemented by replacing the proposed structure with a self-resonance meander line dipole antenna (Fig. 4.9) of the same size as the antenna in parametric matching as

it is shown in Fig. 4.8(b). The passive-loop antenna is matched to 50 Ω and is connected to the spectrum analyzer while the Tx system and its transmit power stays the same. The BW of the passive antenna is measured to be 0.5MHz.

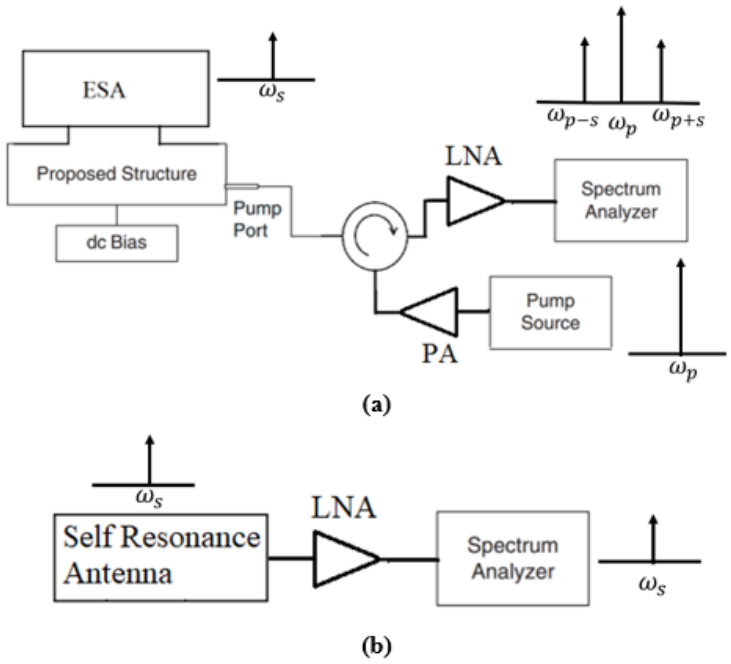

Figure 4.8. The test setup. (a) Parametric matching. (b) Self resonance matching.

Figure 4.9. Fabricated antennas for measurement setup. Self-resonance antenna (Left). Unmatched electrically small bowtie antenna (Right)

C. Measurement Results

The measured received power spectrum for both passive and active cases is shown in Fig. 4.10 for the same power radiated from transmitter. It is evident that antenna with self-resonance matching achieves the highest SNR at antenna passband (52.6MHz) and the SNR is degraded quickly once the operating frequency deviates from the resonance. However, the parametric matching scheme exhibits consistent SNR while the operating frequency moves away from 50MHz, which implies parametric matching offers superior performance when broadband operation is designed even with the ESA on board. In the current parametric matching measurement, the useful frequency band is from 45MHz to 64MHz. The proposed matching network for electrically small bowtie dipole assuming a center frequency of 50MHz has a measured effective efficiency of 25% and a fractional bandwidth of 37%.

The measured SNR improvement over the self-resonance matching is shown in Fig. 4.11. The 3-dB SNR bandwidth for parametric matching is 15MHz while 0.5 MHz for self-resonance antenna leading to BW enhancement of a magnitude of 30 of that in the prototyped structure. It should be noted that the SNR is 7 dB better for ESA with parametric matching over the best case of self-resonance antenna at its passband because the meander line dipole antenna has significantly higher ohmic loss due to its larger radiating metallic part which leads to lower radiation efficiency (4%).

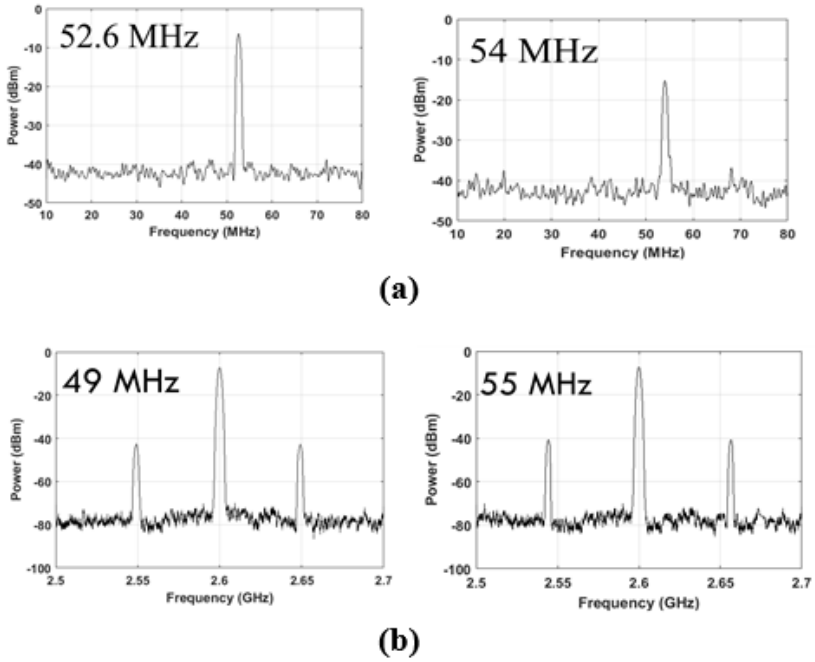

Figure 4.10. The measured spectrum. (a) Self resonance matching. (b) Parametric matching.

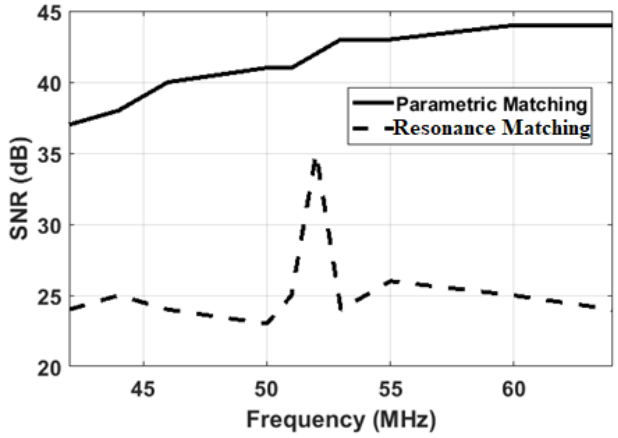

Figure 4.11. Measured SNR improvements of the proposed parametric matching over self-resonance antenna.

Chapter 5

Parametric Power Amplifier for Extended Back-Off Efficiency

5.1 Background of Power Amplifier with Power Back-off Efficiency

The rapid advances in mobile communication systems have led to increasing demands on higher data rates and lower system latency in communication links. Due to the scarcity of spectrum resources, the more efficient digital modulation schemes with even higher peak to average power ratios (PAPRs) such as orthogonal frequency-division multiplexing (OFDM), have been widely exploited in cellular and wireless local area network (WLAN) communications systems. Amplifiers offers the best efficiency at voltage saturation, however, in wireless communication systems because of high order modulation like CDMA, OFDM signals experience high Peak to Average ratio (PAR). Therefore, power amplifier works much below the voltage saturation most of time, resulting in low power efficiency. Therefore, PAs are required to maintain high efficiency over a larger dynamic range from extended back off to saturation.

Several PA architectures are developed in the literates for back-off efficiency enhancement, such as, Doherty PA [58]-[62], outphasing PA [63], envelope-tracking PA [64]-[65], load-modulated balanced PA [66]-[69], and unbalanced power amplifier [70]. The Doherty PA is the most popular architecture in modern communication systems, mainly because of its high efficiency performance achieved at a low hardware complexity and cost level. However, the efficiency of the Doherty PA is enhanced at the cost of linearity deterioration, compared with traditional class A/AB PAs. Therefore, intermodulation cancellation techniques should be done

to satisfy the linearity specification for non-constant envelope modulation. A disadvantage of these linearization is the overhead associated with extra control and tuning circuitry.

The load-modulated balanced amplifier approach is recently proposed to maximize efficiency over extended power back-off where the load impedance modulation is performed using a signal applied to isolation port of hybrid coupler. This architecture has better performance compared to Doherty amplifier; however, the additional signal is needed through an auxiliary amplifier with an external RF signal which must maintain a specific amplitude and phase relationship respect to the RF signal to achieve its goals which needs to use another PA and a wideband phase shifter that can increase the area, efficiency degradation. A modified version of balanced power amplifier is proposed in [67] is composed of two cooperating sub-PAs with the Lange couplers used as the input power splitter and output power combiner. The PA operation is controlled by the transistors' width ratio and coupling coefficients of the couplers. It can, therefore, achieve a broadband operation.

The outphasing PA operates based on a combination of two nonlinear RF PAs, each of which can compensate the efficiency reduction by signal phase control. However, the outphasing PA suffers from a narrow bandwidth and is rarely used in wireless communications. The envelope-tracking PA is sensitive to timing alignment of the envelope signal that can be challenging for wide modulation bandwidths.

To overcome the linearity problem of the above methodologies and to avoid complex control circuitry, it is proposed here to develop a load modulator based on parametric amplification for application with high peak-to-average power ratio. The parametric amplification was well-studied in the 1950s and 1960s to design parametric amplifiers [14]– [19].

However, with the emergence and advancement of the semiconductor technology, the interests of applying parametric effects in electronic applications gradually died out. Recently, there has been a reemergence of interest in parametric amplification effects among microwave circuit designers as parametric circuits consist of only reactive components that enables to design low loss and high energy efficient microwave components. Also, they offer parametric gain by converting pump energy into the signal. Moreover, parametric circuits exhibit time-varying impedance property, which engineers use to design nonreciprocal components [20].

Ideally, for RF signal with high peak to average ratio, a load modulator can be placed after power amplifier to convert the constant load impedance of antenna to an impedance that changes according to the power level (inversely proportional to the output power) as illustrated in Fig. 5.1. Such a load modulator must be low loss and capable of handling a high output power. Therefore, parametric circuits are a good candidate to design load modulator as parametric amplifier converts pump power to the output with approaching to 100% efficiency. Furthermore, the load resistance looking into the pump port is inversely proportional to the converted power as will be discussed in next section.

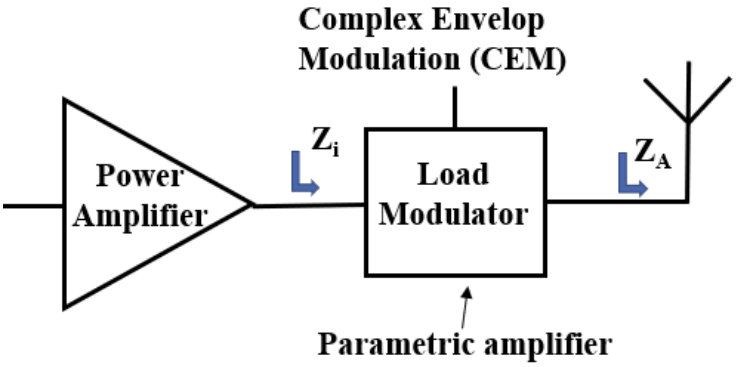

Figure 5.1. Load modulation technique.

5.2 Theory Of Parametric Load Modulator

Parametric amplification is a RF-to-RF conversion process, which relies on non-linear behavior of a varactor under a strong pump voltage. For convenience a lump-element circuit model for a parametric load modulator is shown in Fig. 5.2, which will be used to compute the operating characteristics of the proposed PA.

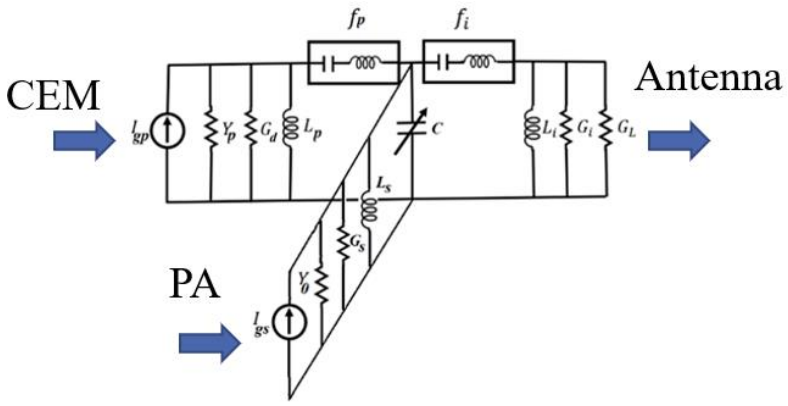

Figure 5.2. Circuit model of the load modulator.

As a matter of definition, the input to the parametric load modulator is typically a complex envelope modulation (CEM) with the frequency of f_s and a pump signal with the frequency of f_p. The output will be at the sum frequency of f_p+f_s. The input circuit is resonant at f_s ,the CEM frequency; one at f_i, the idler frequency; and one at f_p, the pump frequency. It is assumed that all resonant circuits are high Q. Therefore, the significant voltages are developed across resonator only at frequencies close to their resonant frequencies. Input power sources are indicated at the signal frequency and the pump frequency by constant-current generators and associated-shunt conductance. Based on Manley-Rowe relation the energy transferred among different intermodulation can be configured to have different characteristics depend on the termination of

intermodulation tons and harmonics. In the single sideband upconverting mode, a pump voltage at frequency ω_p and a signal at frequency ω_s are applied to the diode, and the output signal is $\omega_p + \omega_s$ taken at the higher frequency as shown in Fig. 5.3. we can summarize the power flow in this circuit with

$$\frac{P_{p+s}}{P_s} = \frac{\omega_{p+s}}{\omega_s} \tag{32}$$

To achieve high gain with an up-converting mode requires a large ratio of output-to-input frequency. In this mode, the power from both signal and pump frequency can be transferred to the idler. Therefore, this operational mode has highest energy efficiency characteristic.

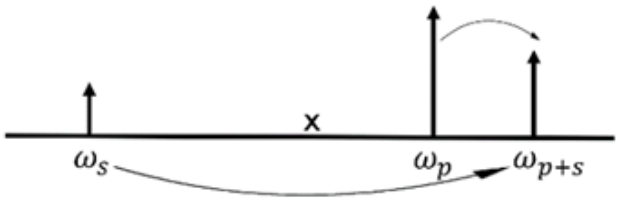

Figure 5.3. Single sideband Upconverting Mode.

A. Determination of the load modulator Characteristic Impedance

Assuming a three-wave mixing case where power flow in and out of a reactance only at three frequencies (f_s, f_i, and f_p) is allowed, therefore, based on Manley and Rowe relations for power flowing into and out of a nonlinear reactance,

$$\frac{P_s}{f_s} + \frac{P_p}{f_p} = 0 \tag{33}$$

$$\frac{P_i}{f_i} + \frac{P_p}{f_p} = 0$$

where $f_i=f_s+f_p$. Therefore, the total pump power injected into the parametric portion of the diode is given by,

$$P_p = \frac{\omega_p}{\omega_i} P_i \tag{34}$$

where P_p and P_i are respectively the total pump power and the power consumed at the idler. Note that the power delivered to the load (P_l) is different than the power consumed at the idler port (P_i) as there is additional power consumed at the diode loss. The total power consumed at the idler port is given by,

$$P_i = \frac{G_l + G_i}{G_l} P_l \tag{35}$$

Therefore, the injected pump power becomes

$$P_p = \frac{G_l + G_i}{G_l} \frac{\omega_p}{\omega_i} P_l \tag{36}$$

If the loss of the diode at the pump port is ignored, the power delivering efficiency is,

$$\frac{P_l}{P_p} = \frac{1}{\left(1 + \frac{G_i}{G_l}\right)} \frac{\omega_i}{\omega_p} \tag{37}$$

It is noted that the power conversion efficiency is a constant and it does not depend on the output power. The effective input admittance at the pump port can also be derived as,

$$G_p = \frac{P_p}{V_p^2} = \frac{1}{V_p^2} \frac{G_l + G_i}{G_l} \frac{\omega_p}{\omega_i} P_l \tag{38}$$

In the parametric power converter, V_p is a constant and the input admittance is thus proportional to the output power delivered to the load. Based on the impedance parametric converter theory presented in [51], the transducer gain in linear region is,

$$\frac{P_l}{P_a} = G_t = \frac{1}{\left(1+\frac{G_s}{Y_0}\right)\left(1+\frac{G_i}{G_l}\right)}\frac{\omega_i}{\omega_s}\cdot\frac{4\gamma^2 Q_s Q_i}{(1+\gamma^2 Q_s Q_i)^2} \tag{39}$$

where $Q_s = \frac{\omega_s C_0}{Y_0+G_s}$ and $Q_i = \frac{\omega_i C_0}{G_i+G_l}$ are, respectively, the loaded factors of signal and idler resonant tanks. Note that P_a and P_l are respectively the available power from the source and the actual power delivered to the load.

Therefore, the injected pump power can be written as,

$$P_p = \frac{1}{\left(1+\frac{G_s}{Y_0}\right)}\frac{\omega_p}{\omega_s}\cdot\frac{4\gamma^2 Q_s Q_i}{(1+\gamma^2 Q_s Q_i)^2}P_a \tag{40}$$

The capacitance modulation index γ is assumed to be linear to the pump voltage before the diode is saturated, which is

$$\gamma \approx kV_p \tag{41}$$

Therefore, the effective input admittance at the pump port is given by,

$$G_p = \frac{P_p}{V_p^2} = \frac{1}{\left(1+\frac{G_s}{Y_0}\right)}\frac{\omega_p}{\omega_s}\cdot\frac{4k^2 Q_s Q_i}{\left(1+k^2 Q_s Q_i V_p^2\right)^2}P_a \tag{42}$$

For a fixed pump voltage, the input admittance is thus found to be proportional to the available source power that is connected to the input of the parametric amplifier.

B. Efficiency of the LMN

Considering the loss of the diode G_d at the pump port, the actual input admittance to the pump source is,

$$G_{p,i} = G_p + G_d = \frac{1}{\left(1+\frac{G_s}{Y_0}\right)}\frac{\omega_p}{\omega_s}\cdot\frac{4k^2Q_sQ_i}{\left(1+k^2Q_sQ_iV_p^2\right)^2}P_a + G_d \tag{43}$$

The total power delivering efficiency is thus,

$$\eta = \frac{P_l}{P_{p,i}} = \frac{1}{\left(1+\frac{G_i}{G_l}\right)\left(1+\frac{G_d}{G_p}\right)}\frac{\omega_i}{\omega_p} \tag{44}$$

The key performance index is

$$\frac{G_d}{G_p} = \frac{\left(1+k^2Q_sQ_iV_p^2\right)^2}{4k^2V_s^2Q_{pu}Q_i}\left(1+\frac{G_s}{Y_0}\right)^2 \tag{45}$$

where Q_{pu} is the unloaded quality factor of the diode at the pump frequency given by,

$$Q_{pu} = \frac{\omega_p C_0}{G_d} \tag{46}$$

Therefore, the circuit can operate at maximum power delivering efficiency mode when $G_p >> G_d$; in fact, the quality factor of diodes is a limited factor of efficiency.

D. Bandwidth limitation

Unlike load modulator in Doherty PA where bandwidth is limited by a frequency-dependent characteristic of the quarter-wavelength transmission line with characteristic impedance of R_{opt}, the fractional bandwidth of proposed load modulator is limited by the bandwidth of the input circuit which is given by

$$b = \frac{1}{Q_s}(1 + \gamma^2 Q_s Q_i) \tag{47}$$

where b is the fractional bandwidth.

C. Linearity

One of the advantages of proposed LMN is to overcome the linearity issue of the load modulator proposed in the literatures, as most load modulators have low IIP3. The linearity of the proposed LMN is determined by the breakdown voltage of the varactor diode. For sake of superior power handling, single varactor may not be able to provide satisfactory performance due to its inherent limitations. However, the breakdown voltage of a diode can be scaled up quite easily by cascading multiple diodes. Therefore, to enhance the power handling of the LMN here, a diodes-stack with 8 varactor diode elements is utilized.

5.3 Experimental Result

The essence of the PPA is based on the dynamic load characteristics of the proposed load, e.g., a RF input signal exhibits different equivalent impedance at the pump port. On the other hand, a PA can achieve its optimum efficiency over a wide range of power level if the load impedance is adjusted inversely proportional to the input power. The schematic and PCB layout of the

proposed parametric PA are shown in Fig. 5.4(a) and (b). The PPA consists of a Class-B amplifier, and a load modulator. The parametric load consists of three series resonators along with a non-linear capacitance. A pump circuit at f_p is indicated by L_p, together with a filter which allows current to flow only at frequency f_p. A similar circuit is shown for the idler frequency. The pump port of load modulator is connected to a Class B amplifier that optimum load condition should be satisfied to obtain maximum efficiency. Therefore, a transmission line with intrinsic impedance of Z_0 with an inductor of L_b is used to create the optimum load for Class B PA at maximum output power.

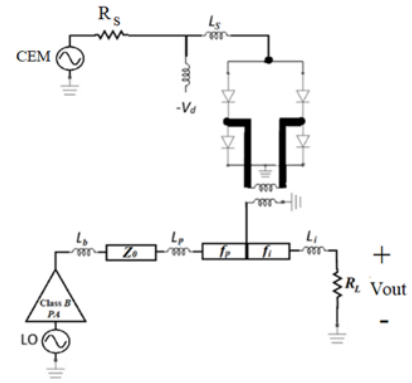

(a)

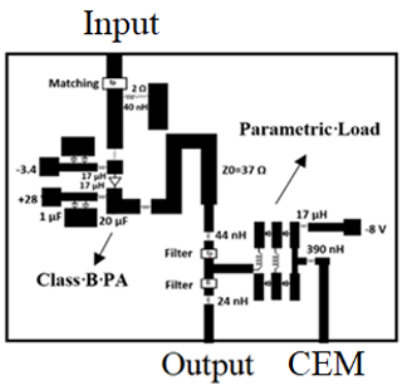

(b)

Figure 5.4. Microstrip parametric PA. (a) Schematic. (b) Layout.

To improve the linearity a diodes-stack with 8 varactor diode elements is utilized which it is shown in Fig. 5.5(a). Their capacitance-versus-voltage behavior is shown in Fig. 5.5(b). It is worth mentioning that each varactor was designed and fabricated with the global communication semiconductors (GCSs) InGaP HBT process and is assembled to the PCB board through wire bonding. It should be noted that the single non-linear capacitor shown in Fig. 5.2 is replaced by a diode bridge for differential operation and strong isolation of the RF signal from the pump and the idler.

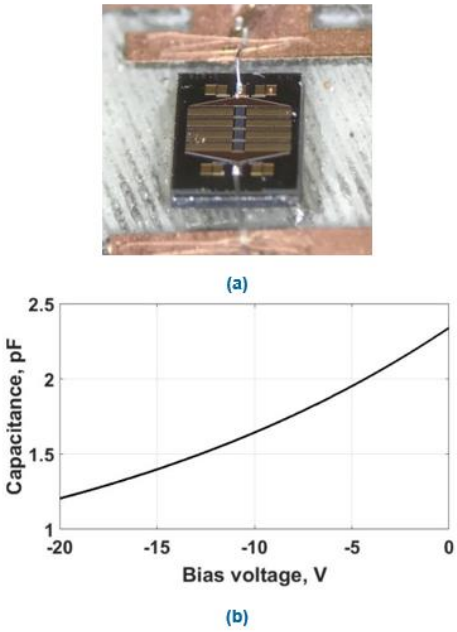

Figure 5.5. Photograph of the stacked diode. (b)Capacitance-versus-voltage of the varactor diode.

To provide the proposed concept, a PPA is designed and fabricated on a Rogers board, which is shown in Fig. 5.6. In the experiment, all varactors are reversely biased with a -8V dc voltage. One inductor with a value of 17 μH is used between signal and dc port to isolate the RF-dc path.

In this setting the RF and pump frequency are set to 220 MHz and 600 MHz. In this design, 10-W GaN HEMT CGH40010 from Cree with -3.3 V gate voltage and 28V drain voltage is used to design the Class B amplifier as a driver of the parametric load to provide 34 dBm driving power for parametric load. Load-pull simulation was performed to obtain the optimal load, which are determined by the tradeoff of output power and efficiency. A transmission line with Z_0=37Ω and one inductor with a value of 12 nH are used between Class B amplifier and the parametric load to satisfy the optimum impedance for Class B amplifier. The stability factor has been used to evaluate the small-signal stability behavior of the amplifier or the desired bias and frequency range. The class B amplifier was stabilized be using a resistor at the input of the gate and a series RL in the gate.

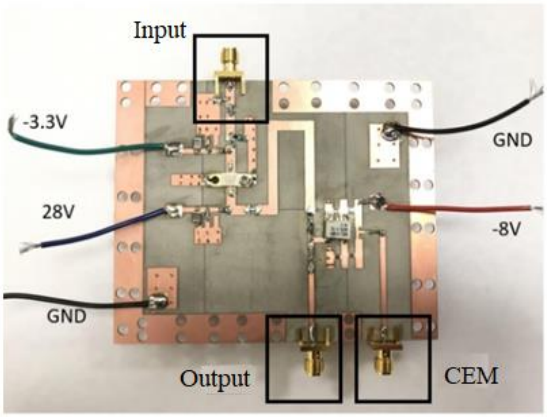

Figure 5.6. Fabricated microstrip parametric power amplifier.

Measured and simulated PAE versus input power at 220 MHz is show in Fig. 5.7. The efficiency here is defined as the ratio between the effective output power from idler port (P_i-P_{in}) and the dc power applied to the Class B amplifier. At 10-dB back off, efficiency of at least 52% can be obtained, while the saturated PAE is 54%. The measured efficiency is around 6% worth than

simulation due to extra loss in fabrication process. Measured parametric gain with respect to the input power is shown in Fig. 5.8. The gain decreases from 5 to 4 dB with varying output power with the compression point at saturation. The saturation output power is 32 dBm. The maximum efficiency versus frequency is shown in Fig. 5.9. The PPA achieves a high maximum efficiency of 45%-50% over 190 MHz-242 MHz. It should be noted that the primary purpose of this design is to demonstrate the proposed concept, and the presented prototype is a first-pass design. Realistically, the bandwidth can be improved with more design iterations.

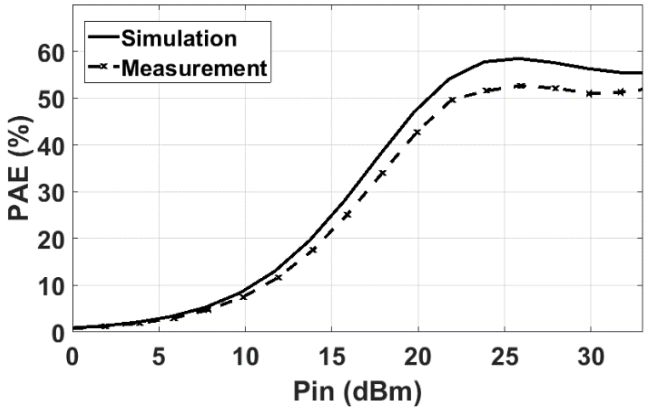

Figure 5.7. Simulated and measured PAE versus input power at 220 MHz.

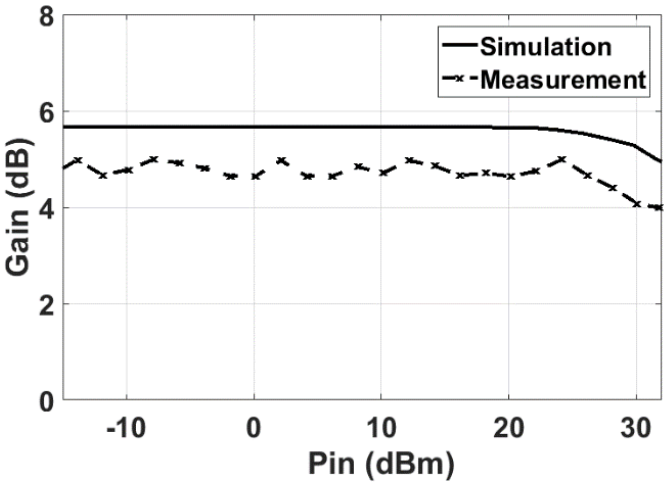

Figure 5.8. Simulation and measurement of gain versus input power at 220 MHz.

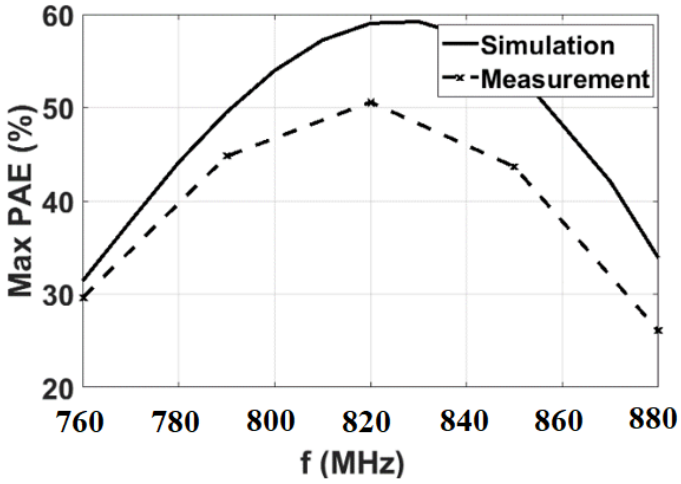

Figure 5.9. Simulation and measurement of maximum PAE frequency.

Chapter 6

Summary

6.1 Conclusion

In this dissertation, author has been developed, characterized the concept of parametroincs, and demonstrated of novel parametric architectures capable of efficient, low noise and wideband operation. First, theory of parametric amplification was explored and to further analysis of the parametric circuit, we have shown, how a nonlinear capacitance can be well presented by linear time variant capacitance.

In this work, three different RF and microwave components based parametric amplification concept, are successfully proposed, designed, and fabricated.

As the first design, we proposed a low noise mixer-first architecture based on a parametric downconverter. The theory on the characteristics of parametric downconverters with gain and low noise figure has been discussed. As proof-of-concept mixer is fabricated on the PCB and is successfully measured. The fabricated mixer achieves a maximum conversion gain of 10 dB and a minimum noise figure of 2.8 dB within the frequency band of interest with +16 dBm IIP3. The design in this paper is only a preliminary design to prove the concept. The parametric mixer has the potential of becoming a low noise, high P1dB downconverter for “mixer first” receivers comparing to the conventional mixers.

Then, we presented the design and experimental characterization of a novel matching technique for receivers with ESA so that the receiver can achieve low noise performance over a broad bandwidth. We proposed to incorporate the ESA as part of the circuit and analyzed the

noise figure from the wave port of the antenna to the output of the LNA. This has be done by replacing the ESA with Chu's equivalent circuit and treat the radiation resistance as the source resistance for noise figure calculation. The complete theory of parametric matching is also presented which has been validated with the nonlinear circuit simulation results. Finally, the structure was prototyped, and measured SNR were compared to the self-resonance matched antenna. We have shown that parametric matching approach can offer significant SNR improvements over self-resonance matching techniques when wideband operation is desired.

Finally, we proposed an efficient way to design power amplifiers with broadband power back-off efficiency based on a parametric load. The theory on the characteristics of parametric load has been discussed and as the proof-of-concept power amplifier is fabricated on the PCB and is successfully measured, the fabricated PA achieves 10-dB back off, efficiency of at least 52% with 32 dBm output power. Comparing to conventional Class-B operation mode, the PPA offers significantly improved power efficiency versus power back-off curves.

Appendix

Appendix A.

The aim of this appendix is to provide some mathematical details to understand the proposed parametric downconverter. Transducer power gain and noise figure can be derived based on the circuit model shown in Fig. A1. A signal circuit at f_s is indicated by B_s, together with a filter which allows current to flow only at the signal frequency. A similar circuit B_i+ G_l is shown for the output frequency. I_{g1} and I_{g2} are current sources (defined in rms values) at the input and output ports of the mixer, respectively. Also, with the assumption of pump power much greater than signal power, the pumped nonlinear capacitor can be modeled by a small-signal admittance matrix, as shown in (17),

$$\begin{pmatrix} I_s \\ I_i^* \end{pmatrix} = \begin{pmatrix} Y_{11} & Y_{12} \\ Y_{21} & Y_{22} \end{pmatrix} \begin{pmatrix} V_s \\ V_i^* \end{pmatrix} = \begin{pmatrix} j\omega_s C_0 & j\omega_s \gamma C_0 \\ -j\omega_i \gamma C_0 & -j\omega_i C_0 \end{pmatrix} \begin{pmatrix} V_s \\ V_i^* \end{pmatrix}. \tag{A1}$$

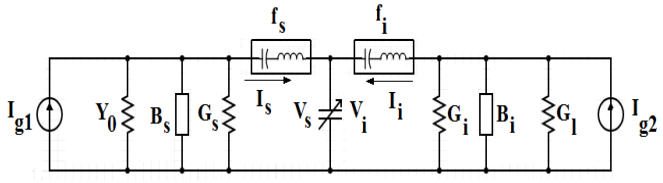

Figure A.1: Circuit model used in the analysis of the downconverter.

Now, for conceptual purposes and to calculate transducer gain based on the small-signal model, the equivalent circuit can be redrawn as the one shown in Fig. A2.

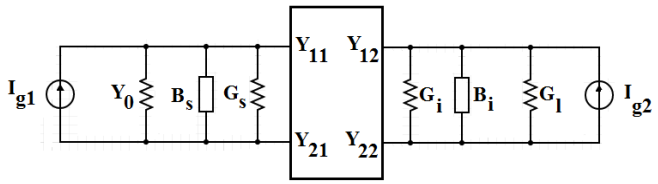

Figure A.2: Linear four terminal representation of the downconverter.

Firstly, at resonance, the idler tank becomes an open circuit, and the power dissipated on the load is,

$$P_{load} = V_i^2 G_l. \tag{A2}$$

Also, the available power from the signal current source is given by,

$$P_{source} = \frac{|I_{g1}|^2}{4Y_0}. \tag{A3}$$

Based on the standard linear circuit techniques the transducer gain can be written as the ratio of the actual power output to the available input power. Therefore, the transducer gain is,

$$G_t = \frac{4Y_0 G_l V_i^2}{|I_{g1}|^2}. \tag{A4}$$

To calculate the transducer gain, it is necessary to express I_{g1} in terms of V_i. This is accomplished in the matrix formulation by adding the external circuit admittances to the effective self-impedances of the nonlinear capacitor. Therefore, we have,

$$\begin{pmatrix} I_{g1} \\ I_{g2}^* \end{pmatrix} = \begin{pmatrix} Y_{11}+B_s+Y_0+G_s & Y_{12} \\ Y_{21} & Y_{22}+B_i+G_i+G_l \end{pmatrix} \begin{pmatrix} V_s \\ V_i^* \end{pmatrix} \quad (A5)$$

The current I_{g1} can be easily obtained by setting $I_{g2}^* = 0$. The transducer gain then becomes,

$$G_t = \frac{4Y_0 G_l |Y_{21}|^2}{|(Y_{11}+Y_{T1})(Y_{22}+Y_{T2}{}^*) - Y_{12}Y_{21}|^2} \quad (A6)$$

where $Y_{T1} = B_s + Y_0 + G_s$ and $Y_{T2} = B_i + G_i + G_l$. To investigate the mid-band gain, the tuning conditions are imposed as

$$-B_s = Y_{11}, -B_i = Y_{22}. \quad (A7)$$

Therefore, at resonance then, the gain becomes,

$$G_t = \frac{4Y_0 G_l \gamma^2 \omega_i{}^2 C_0{}^2}{(Y_0+G_s)^2 (G_i+G_l)^2 \left(1 - \frac{\omega_s \omega_i C_0{}^2 \gamma^2}{(Y_0+G_s)(G_i+G_l)}\right)^2}. \quad (A8)$$

This expression can be further simplified to,

$$G_t = \frac{1}{\left(1+\frac{G_s}{Y_0}\right)\left(1+\frac{G_i}{G_l}\right)} \frac{\omega_i}{\omega_s} \cdot \frac{4\gamma^2 Q_s Q_i}{(1-\gamma^2 Q_s Q_i)^2} \quad (A9)$$

where $Q_s = \frac{\omega_s C_0}{Y_0+G_s}$ and $Q_i = \frac{\omega_i C_0}{G_i+G_l}$ are, respectively, the loaded factors of signal and idler resonant tanks. For low noise condition, the signal resonator admittance G_s and the idler resonator admittance G_i should be chosen much smaller than the source admittance Y_0 and the load conductance G_l ($G_s \ll Y_0$ and $G_i \ll G_l$). In this case, the gain is derived to be,

$$G_a = \frac{\omega_i}{\omega_s} \cdot \frac{4\gamma^2 Q_s Q_i}{(1-\gamma^2 Q_s Q_i)^2}. \tag{A10}$$

To derive the noise figure expression, current sources at both signal and idler frequencies will be used to represent thermal noise. We must evaluate the noise power delivered to the load when Y_0 is at the temperature (T_0) of 290°K. The output noise power can be derived based on the matrix equation (A5). Replacing I_{g1} by the noise current i_{ns}, and setting I_{g2} =0, the noise power delivered to the load G_l due to the thermal source at f_s is,

$$N_s = \frac{i_{ns}^2 G_l |Y_{21}|^2}{|(Y_{11}+Y_{T1})(Y_{22}+Y_{T2}^*) - Y_{12}Y_{21}|^2}. \tag{A11}$$

Similarly, for the noise source at f_i is,

$$N_i = \frac{i_{ni}^2 G_l |Y_{11}+Y_{T1}^*|^2}{|(Y_{11}+Y_{T1})(Y_{22}+Y_{T2}^*) - Y_{12}Y_{21}|^2} \tag{A12}$$

where Y_{ij}'s are admittance matrix elements given in (A1). The thermal noise currents at f_s and f_i are,

$$i_{ns}^2 = 4KT_0B(Y_0+G_s) \text{ and } i_{ni}^2 = 4KT_0B(G_i). \tag{A13}$$

The total noise power is the sum of N_s and N_i.

$$N_o = N_s + N_i. \tag{A14}$$

The noise figure then is,

$$F = \frac{N_o}{G_t k T_0 B} = \frac{1}{4kT_0BY_0}\left(i_{ns}^2 + \frac{(Y_0+G_s)^2}{\omega_i^2\gamma^2 C_0^2} i_{ni}^2\right). \tag{A15}$$

This expression can be further simplified to,

$$F_N = \left(1 + \frac{G_s}{Y_0}\right)\left(1 + \frac{\omega_s}{\omega_i}\frac{1}{\gamma^2 Q_s Q_{iu}}\right) \tag{A16}$$

where Q_s and Q_{iu} are loaded and unloaded quality factor of signal and idler loop, respectively, with $Q_{iu} = \frac{\omega_i C_0}{G_i}$.

The fractional bandwidth relation given in (22) can be obtained by first expressing $Y_0 + G_s$and $G_i + G_l$ around the signal and idler frequencies, respectively, as

$$Y_0 + G_s \rightarrow Y_0 + G_s(1 + j2\delta_s Q_s), \tag{A17}$$

$$G_i + G_l \rightarrow G_i + G_l(1 - j2\delta_i Q_i)$$

with $\delta_s = \Delta\omega_s/\omega_s$, $\delta_i = \Delta\omega_i/\omega_i$. The transducer gain becomes,

$$G_t = \frac{\frac{4Y_0 G_l \gamma^2 {\omega_i}^2 {C_0}^2}{((Y_0 + G_s)(G_i + G_l))^2}}{\left\{1 + 4\delta_s Q_s \delta_i Q_i - \frac{\omega_s \omega_i {C_0}^2 \gamma^2}{(Y_0 + G_s)(G_i + G_l)}\right\}^2 + \{2(\delta_s Q_s - \delta_i Q_i)\}^2} \tag{A18}$$

where $\delta_i = -\frac{\omega_s}{\omega_i}\delta_s$.

This expression can be further simplified to,

$$G_t = \frac{\frac{4Y_0 G_l \gamma^2 {\omega_i}^2 {C_0}^2}{((Y_0 + G_s)(G_i + G_l))^2}}{\left\{1 - \frac{\omega_s \omega_i {C_0}^2 \gamma^2}{(Y_0 + G_s)(G_i + G_l)} - (2\delta_s Q_s)^2 \frac{\omega_s}{\omega_i}\frac{Q_i}{Q_s}\right\}^2 + (2\delta_s Q_s)^2 \left\{1 + \frac{\omega_s}{\omega_i}\frac{Q_i}{Q_s}\right\}^2} \tag{A19}$$

Setting the denominator of (A19) equal to twice its resonant value, we obtain the following quadratic equation,

$$c^2s^2 + (c^2 - 2ac + 1)s - (1 - a)^2 = 0 \tag{A20}$$

where $s = (2\delta_s Q_s)^2$, $a = \frac{\omega_s \omega_i {C_0}^2 \gamma^2}{(Y_0 + G_s)(G_i + G_l)}$, and $c = \frac{\omega_s}{\omega_i}\frac{Q_i}{Q_s}$.

The fractional bandwidth of the downconverter is $2\delta_s$, while the fractional bandwidth of the input resonant circuit is $1/Q_s$. Therefore, the parameter *s* represents the ratio of downconverter bandwidth to input circuit bandwidth. In the general case, the fractional bandwidth of downconverter can be computed from (A20). As an example and to simplify matters, an approximate solution will be used. Assume Q_s and Q_i are chosen based on equation (A20), somehow c is small compared to unity, so

$$s = (1 - a)^2 \tag{A21}$$

therefore,

$$b = \frac{1}{Q_s}(1 - a). \tag{A22}$$

This expression can be written as,

$$b = \frac{1}{Q_s}(1 - \gamma^2 Q_i Q_s) \tag{A23}$$

where $b = 2\delta_s$ is the fractional bandwidth.

Appendix B.

The aim of this appendix is to provide some mathematical details to understand the proposed parametric matching. The transducer power gain and NF can be derived based on the circuit model shown in Fig. B1.

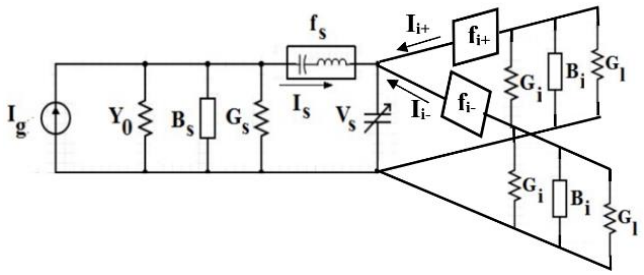

Figure B.1: Schematic of parametric amplifier with arbitrary source and load for theoretical analyses.

Y_0 is the source conductance of the antenna and G_s is the equivalent shunt conductance on the signal side which represents the loss of the diode reflected onto the signal side. G_l is the load conductance and G_i represents the equivalent shunt conductance of the diode on the idler side. The cross-frequency admittance matrix [51] is thus given by,

$$\begin{pmatrix} I_s \\ I_{i-}^* \\ I_{i+} \end{pmatrix} = \begin{pmatrix} j\omega_s C_0 & j\omega_s \gamma C_0 & j\omega_s \gamma C_0 \\ -j\omega_{i-}\gamma C_0 & -j\omega_{i-} C_0 & 0 \\ j\omega_{\iota+}\gamma C_0 & 0 & j\omega_{i+} C_0 \end{pmatrix} \begin{pmatrix} V_s \\ V_{i-}^* \\ V_{i+} \end{pmatrix} \qquad (B1)$$

where $V_s, I_s, V_{i-}, I_{i-}, V_{i+}, I_{i+}$ are voltages and currents for the signal, the lower sideband of idler and the upper sideband of the idler. The transducer gain from the signal to the idler port is thus,

$$G_t = \frac{4Y_0 G_l V_i^2}{\left|I_g\right|^2}. \qquad (B2)$$

On the idler port, both sidebands have the termination condition that defines,

$$\begin{cases} I_{i-}^{*} = -(G_i + G_l - jB_i)V_{i-}^{*} \\ I_{i+} = -(G_i + G_l + jB_i)V_{i+} \end{cases} \tag{B3}$$

Substituting (*B*3) into the last two equations of (*B*1) yields,

$$\begin{cases} V_{i-}^{*} = \dfrac{j\omega_{i-}\gamma C_0}{G_i + G_l - jB_i - j\omega_{i-}C_0} V_s \\ V_{i+} = -\dfrac{j\omega_{i+}\gamma C_0}{G_i + G_l + jB_i + j\omega_{i+}C_0} V_s \end{cases} \tag{B4}$$

With a narrow band assumption at the upconverted frequencies, both idlers are resonant so that the reactance in the denominators disappear, the following relation approximately holds,

$$V_{i-}^{*} + V_{i+} = 0 \tag{B5}$$

This leads to a simplification of the first equation in (B1), which becomes,

$$I_s = j\omega_s C_0 V_s + j\omega_s \gamma C_0 (V_{i-}^{*} + V_{i+}) = j\omega_s C_0 V_s \tag{B6}$$

The input current is thus yielded as

$$|I_g| = \left| I_s + (Y_0 + G_s + jB_s)V_s = \left| (Y_0 + G_s + jB_s + j\omega_s C_0) \frac{G_i + G_l}{j\omega_i \gamma C_0 V_i} \right| \right. \tag{B7}$$

Substituting it into (*B*2) leads to the transducer gain expression,

$$G_T = \frac{4Y_0 G_l \gamma^2 {\omega_i}^2 {C_0}^2}{|Y_0 + G_s + jB_s + j\omega_s C_0|^2 (G_i + G_l)^2}. \tag{B8}$$

When the parametric amplifier is directly connected to an electrically small dipole represented by its Chu's equivalence and next the series RC approximation, one can define the radiation quality factor of the antenna and the intrinsic quality factor of the varactor diode at the original signal frequency as,

$$Q_a = \frac{B_s}{Y_0}, Q_d = \frac{\omega_s C_0}{G_s} \tag{B9}$$

The idler output assumes a conjugate match with $G_i = G_l$, the transducer gain then becomes,

$$G_T = \frac{Y_0 G_s}{(Q_a Y_0 + Q_d G_s)^2} \frac{\omega_i C_0}{G_s} \frac{\omega_i C_0}{G_i} \gamma^2 \tag{B10}$$

Note that the varactor diode quality factor is inversely proportional to its operating frequency, at the idler frequency, it satisfies $Q_{d,\omega_i} = \frac{\omega_i C_0}{G_i} = \frac{\omega_s}{\omega_i} Q_d$. The transducer equation (*B*10) thus becomes,

$$G_T = \frac{Y_0 G_s}{(Q_a Y_0 + Q_d G_s)^2} Q_d^2 \gamma^2 \tag{B11}$$

One can prove that the transducer gain is maximized when the following holds,

$$Q_a Y_0 = Q_d G_s \tag{B12}$$

This optimum matching condition gives,

$$\omega_s C_a = \omega_s C_0 \; or \; C_a = C_0 \tag{B13}$$

Substituting (*B*13) into (*B*11) and considering both single side band and double side band cases, the maximized transducer gain is thus,

$$G_{T,max} = \frac{1}{2}\frac{Q_d}{Q_a}\gamma^2 \qquad (B14)$$

To derive the noise figure expression, current sources at both signal and idler frequencies will be used to represent thermal noise. The noise power delivered to the load G_l due to the thermal source at the signal frequency f_s is,

$$N_s = \frac{G_T i_{ns}^2}{4Y_0} \qquad (B15)$$

Similarly, for the noise source at the idler frequency f_i is,

$$N_i = \frac{i_{ni}^2}{(G_i + G_l)^2} G_l \qquad (B16)$$

The thermal noise currents at f_s and f_i are,

$$i_{ns}^2 = 4KT_0B(Y_0 + G_s) \text{ and } i_{ni}^2 = 4KT_0B(G_i). \qquad (B17)$$

The total noise power is the sum of N_s and N_i.

$$N_o = N_s + N_i. \qquad (B18)$$

The noise figure then is,

$$F = \frac{N_o}{G_T k T_0 B} = \frac{1}{kT_0B}\left(\frac{i_{ns}^2}{4Y_0} + \frac{1}{G_T}\frac{i_{ni}^2}{(G_i + G_l)^2} G_l\right). \qquad (B19)$$

This expression can be further simplified to,

$$F_N = 1 + \frac{G_s}{Y_0} + \frac{1}{G_T}\frac{4G_iG_l}{(G_i + G_l)^2} \qquad (B20)$$

Under the maximum gain condition, the noise figure thus becomes,

$$F_N = 1 + \frac{G_s}{Y_0} + \frac{1}{G_T} = 1 + \frac{Q_a}{Q_d}\left(1 + \frac{2}{\gamma^2}\right) \qquad (B21)$$

References

[1] F. Lin, P.-I. Mak, and R. P. Martins, “Wideband receivers: design challenges, tradeoffs and state-of-the-art,” *IEEE Circuits Syst. Mag.*, vol. 15, no. 1, pp. 12–24, 2015.

[2] D. Murphy, H. Darabi, A. Abidi, A. A. Hafez, A. Mirzaei, M. Mikhemar, and M.-C. F. Chang, “A blocker-tolerant, noise-cancelling receiver suitable for wideband wireless applications,” *IEEE J. Solid-State Circuits*, vol. 47, no. 12, pp. 2943–2963, 2012.

[3] J. Tao, X. Fan, and X. Chen, “A SAW-less receiver front-end with continuously variable bandwidth and enhanced blocker-filtering,” *IEICE Electron. Express*, vol. 15, no. 12, pp. 1–12, 2018.

[4] A. Ghaffari, E. A. M. Klumperink, M. C. M. Soer, and B. Nauta, “Tunable high-Q N-path band-pass filters: Modeling and verification,” *IEEE J. Solid-State Circuits*, vol. 46, no. 5, pp. 998–1010, 2011.

[5] B. van Liempd, J. Borremans, E. Martens, S. Cha, H. Suys, B. Verbruggen, and J. Craninckx, “A 0.9 V 0.4–6 GHz harmonic recombination SDR receiver in 28 nm CMOS with HR3/HR5 and IIP2 calibration,” *IEEE J. Solid-State Circuits*, vol. 49, no. 8, pp. 1815–1826, 2014.

[6] A. Mirzaei, H. Darabi, A. Yazdi, Z. Zhou, E. Chang, and P. Suri, “A 65 nm CMOS quad-band SAW-less receiver SoC for GSM/GPRS/EDGE,” *IEEE J. Solid-State Circuits*, vol. 46, no. 4, pp. 950–964, 2011.

[7] L. Duipmans, R. E. Struiksma, E. A. M. Klumperink, B. Nauta, and F. E. van Vliet, “Analysis of the signal transfer and folding in N-path filters with a series inductance,” *IEEE Trans. circuits Syst. I Regul. Pap.*, vol. 62, no. 1, pp. 263–272, 2014.

[8] K. B. Östman, M. Englund, O. Viitala, M. Kaltiokallio, K. Stadius, K. Koli, and J. Ryynanen, "Analysis and design of N-path filter offset tuning in a 0.7–2.7-GHz receiver front-end," *IEEE Trans. Circuits Syst. I Regul. Pap.*, vol. 62, no. 1, pp. 234–243, 2014.

[9] F. Qazi and J. Dąbrowski, "Clock phase imbalance and phase noise in RF N-path filters," in *2015 European Conference on Circuit Theory and Design (ECCTD)*, 2015, pp. 1–4.

[10] J. W. Park and B. Razavi, "Channel selection at RF using miller bandpass filters," *IEEE J. Solid-State Circuits*, vol. 49, no. 12, pp. 3063–3078, 2014.

[11] A. Nejdel, M. Abdulaziz, M. Törmänen, and H. Sjöland, "A positive feedback passive mixer-first receiver front-end," in *2015 IEEE Radio Frequency Integrated Circuits Symposium (RFIC)*, 2015, pp. 79–82.

[12] M. H. Kashani, A. Tarkeshdouz, E. Afshari, and S. Mirabbasi, "A 53–67 GHz low-noise mixer-first receiver front-end in 65-nm CMOS," *IEEE Trans. Circuits Syst. I Regul. Pap.*, vol. 66, no. 6, pp. 2051–2063, 2019.

[13] R. Ying, M. Morton, and A. Molnar, "A HBT-based 300 MHz-12 GHz blocker-tolerant mixer-first receiver," in *ESSCIRC 2017-43rd IEEE European Solid State Circuits Conference*, 2017, pp. 31–34.

[14] P. K. Tien and H. Suhl, "A Traveling-Wave Ferromagnetic Amplifier," *Proc. IRE*, vol. 46, no. 4, pp. 700-706, April 1958.

[15] Tien, P. K. "Parametric amplification and frequency mixing in propagating circuits." *J. Appl. Phys.* vol. 29, no. 9, pp. 1347-1357, Sep. 1958.

[16] A. Cullen, "A Travelling-Wave Parametric Amplifier", *Nature*, vol. 181, no. 4605, pp. 332-332, 1958.

[17] H. Heffner and G. Wade, "Gain, Band Width, and Noise Characteristics of the Variable-Parameter Amplifier", *J. Appl. Phys.*, vol. 29, no. 9, pp. 1321-1331, 1958.

[18] J. Edrich, "Low-noise parametric amplifiers tunable over one full octave," *IEEE J. Solid-State Circuits*, vol. 7, no. 1, pp. 32-37, Feb. 1972.

[19] A. Smith, R. Sandell, J. Burch, and A. Silver, "Low noise microwave parametric amplifier," *IEEE Trans. Magn.*, vol. 21, no. 2, pp. 1022-1028, March 1985.

[20] S. Qin, Q. Xu, and Y. E. Wang, "Nonreciprocal components with distributedly modulated capacitors," *IEEE Trans. Microw. Theory Tech.*, vol. 62, no. 10, pp. 2260–2272, 2014.

[21] W. Lee and E. Afshari, "Low-Noise Parametric Resonant Amplifier," *IEEE Trans. Circuits Syst. I: Reg. Papers*, vol. 58, no. 3, pp. 479-492, March 2011.

[22] B. Gray, "Design of RF and Microwave Parametric Amplifiers and Power Upconverters", Ph.D. dissertation, School of Elect. and Comp. Eng., Georgia Inst. of Tech., USA, 2012 [Online]. Available: https://smartech.gatech.edu/handle/1853/43613

[23] Z. Zhao, S. Magierowski and L. Belostotski, "Parametric CMOS upconverters and downconverters", *Int. J. Circ. Theor. App.*, vol. 42, no. 12, pp. 1209-1227, 2013.

[24] B. Gray, M. Pontón, A. Suárez, and J. S. Kenney, "Analytical modeling of transducer gain and gain compression in degenerate parametric amplifiers," in *2012 IEEE Radio and Wireless Symposium*, 2012, pp. 351–354.

[25] B. Gray, F. Ramirez, B. Melville, A. Suarez, and J. S. Kenney, "A broadband double-balanced phase-coherent degenerate parametric amplifier," *IEEE Microw. Wirel. components Lett.*, vol. 21, no. 11, pp. 607–609, 2011.

[26] Q. Wu, X. Zou, S. Qin, and Y. E. Wang, “Frequency translational RF receiver with time varying transmission lines (TVTL),” in *2017 IEEE MTT-S International Microwave Symposium (IMS)*, 2017, pp. 1767–1769.

[27] J. M. Manley and H. E. Rowe, "Some General Properties of Nonlinear Elements-Part I. General Energy Relations," *Proc. IRE*, vol. 44, no. 7, pp. 904-913, July 1956.

[28] B. Gray, M. Ponton, A. Suarez, and J. S. Kenney, “A phase-coherent upconverting parametric amplifier,” *IEEE Microw. Wirel. components Lett.*, vol. 22, no. 10, pp. 527–529, 2012.

[29] B. Gray, B. Melville, and J. S. Kenney, “Analytical modeling of microwave parametric upconverters,” *IEEE Trans. Microw. Theory Tech.*, vol. 58, no. 8, pp. 2118–2124, 2010.

[30] S. Magierowski, J.-F. Bousquet, Z. Zhao, and T. Zourntos, “RF CMOS parametric downconverters,” *IEEE Trans. Microw. Theory Tech.*, vol. 58, no. 3, pp. 518–528, 2010.

[31] H. Trabelsi and C. Cruchon, “A varactor-tuned active microwave bandpass filter,” *IEEE Microwave Guided Wave Lett.*, vol. 2, no. 6, pp. 231–232, 1992.

[32] X. Zou, Q. Wu, and Y. E. Wang, “Monolithically Integrated Parametric Mixers With Time-Varying Transmission Lines (TVTLs),” *IEEE Trans. Microw. Theory Tech.*, vol. 68, no. 10, pp. 4479–4490, 2020.

[33] S. C. Blaakmeer, E. A. M. Klumperink, D. M. W. Leenaerts, and B. Nauta, “The BLIXER, a wideband balun-LNA-I/Q-mixer topology,” *IEEE J. Solid-State Circuits*, vol. 43, no. 12, pp. 2706–2715, 2008.

[34] N. Kim, V. Aparin, and L. E. Larson, “A Resistively Degenerated Wideband Passive Mixer With Low Noise Figure and High IIP2*,” IEEE Trans. Microw. Theory Tech*., vol. 58, no. 4, pp. 820–830, 2010.

[35] S. S. K. Ho and C. E. Saavedra, “A CMOS broadband low-noise mixer with noise cancellation,” *IEEE Trans. Microw. Theory Tech.*, vol. 58, no. 5, pp. 1126–1132, 2010.

[36] D. Na and T. W. Kim, “A 1.2 V, 0.87–3.7 GHz wideband low-noise mixer using a current mirror for multiband application,” *IEEE Microw. Wirel. components Lett*., vol. 22, no. 2, pp. 91–93, 2012.

[37] J.-Y. Lee, J.-Y. Park, and T.-Y. Yun, “Flicker noise improved CMOS mixer using feedback current bleeding,” *IEEE Microw. Wirel. Components Lett.*, vol. 27, no. 8, pp. 730–732, 2017.

[38] B. Guo, H. Wang, and G. Yang, “A wideband merged CMOS active mixer exploiting noise cancellation and linearity enhancement,” *IEEE Trans. Microw. Theory Tech.*, vol. 62, no. 9, pp. 2084–2091, 2014.

[39] A. V. Gurevich and E. E. Tsedilina, *Long distance propagation of HF radio waves*. Springer, 1985.

[40] L. J. Chu, “Physical limitations of omni-directional antennas,” *J. Appl. Phys.*, vol. 19, no. 12, pp. 1163–1175, 1948.

[41] H. A. Wheeler, “Fundamental limitations of small antennas,” *Proc. IRE*, vol. 35, no. 12, pp. 1479–1484, 1947.

[42] R. M. Fano, “Theoretical limitations on the broadband matching of arbitrary impedances,” *J. Franklin Inst.*, vol. 249, no. 1, pp. 57–83, 1950.

[43] M. Manteghi, “Fundamental limits, bandwidth, and information rate of electrically small antennas: Increasing the throughput of an antenna without violating the thermodynamic Q-factor,” *IEEE Antennas Propag. Mag.*, vol. 61, no. 3, pp. 14–26, 2019.

[44] H. Wolff, “High-speed frequency-shift keying of LF and VLF radio circuits,” *IRE Trans. Commun. Syst.*, vol. 5, no. 3, pp. 29–42, 1957.

[45] M. Manteghi, “An electrically small antenna concept design for transmitting a baseband signal,” in *2017 IEEE International Symposium on Antennas and Propagation & USNC/URSI National Radio Science Meeting*, 2017, pp. 1481–1482.

[46] S. E. Sussman-Fort and R. M. Rudish, “Non-Foster impedance matching of electrically-small antennas,” *IEEE Trans. Antennas Propag.*, vol. 57, no. 8, pp. 2230–2241, 2009.

[47] S. E. Sussman-Fort and R. M. Rudish, “Non-Foster impedance matching for transmit applications,” in *IEEE International Workshop on Antenna Technology Small Antennas and Novel Metamaterials, 2006.*, 2006, pp. 53–56.

[48] K.-S. Song and R. G. Rojas, “Non-Foster impedance matching of electrically small antennas,” in *2010 IEEE Antennas and Propagation Society International Symposium*, 2010, pp. 1–4.

[49] J. T. Aberle, “Two-port representation of an antenna with application to non-foster matching networks,” *IEEE Trans. Antennas Propag.*, vol. 56, no. 5, pp. 1218–1222, 2008.

[50] L. K. Yeung, X. Zou, and Y. Wang, “Parametrically enhanced bandpass filters,” IET Microwaves, Antennas Propag., vol. 15, no. 2, pp. 229–240, 2021.

[51] M. Hedayati, L. K. Yeung, M. Panahi, X. Zou, and Y. E. Wang, “Parametric Downconverter for Mixer-First Receiver Front Ends,” IEEE Trans. Microw. Theory Tech., vol. 69, no. 5, pp. 2712–2721, 2021.

[52] P. Loghmannia and M. Manteghi, “An active cavity-backed slot antenna based on a parametric amplifier,” *IEEE Trans. Antennas Propag.*, vol. 67, no. 10, pp. 6325–6333, 2019.

[53] H. Li, A. Mekawy, and A. Alù, “Beyond Chu’s limit with Floquet impedance matching,” *Phys. Rev. Lett.*, vol. 123, no. 16, p. 164102, 2019.

[54] P. Loghmannia and M. Manteghi, “Broadband parametric impedance matching for small antennas using the Bode-Fano limit,” *IEEE Antennas and Propagation Magazine*, pp.2-15, July, 2021.

[55] K. Q. T. Luong, W. Gu, F. Fereidoony, L. Yeung, Z. Yao, and Y. E. Wang, “Radio Frequency Precession Modulation Based Magnetic Field Sensors,” *IEEE Access*, 2022.

[56] S. R. Best, “Optimizing the receiving properties of electrically small HF antennas,” *URSI Radio Sci. Bull.*, vol. 2016, no. 359, pp. 13–29, 2016.

[57] R. E. Collin, “Parametric amplifiers,” 2001.

[58] G. Nikandish, R. B. Staszewski, and A. Zhu, “Breaking the bandwidth limit: A review of broadband Doherty power amplifier design for 5G,” *IEEE Microw. Mag.*, vol. 21, no. 4, pp. 57–75, 2020.

[59] V. Vorapipat, C. S. Levy, and P. M. Asbeck, “Voltage mode Doherty power amplifier,” *IEEE J. Solid-State Circuits*, vol. 52, no. 5, pp. 1295–1304, 2017.

[60] V. Vorapipat, C. S. Levy, and P. M. AsbeckIEEE, “A class-G voltage-mode Doherty power amplifier,” *IEEE J. Solid-State Circuits*, vol. 52, no. 12, pp. 3348–3360, 2017.

[61] A. N. Kangarshahi and A. Zahedi, “High Efficiency and High Output Power HFET GaN Doherty Power Amplifier with Linearity Region Extension for Wireless Applications,” *Circuits, Syst. Signal Process.*, pp. 1–19, 2022.

[62] Y. Xu, J. Pang, X. Wang, and A. Zhu, “Enhancing bandwidth and back-off range of Doherty power amplifier with modified load modulation network,” *IEEE Trans. Microw. Theory Tech.*, vol. 69, no. 4, pp. 2291–2303, 2021.

[63] X. A. Nghiem, J. Guan, and R. Negra, “Broadband sequential power amplifier with Doherty-type active load modulation,” *IEEE Trans. Microw. Theory Tech.*, vol. 63, no. 9, pp. 2821–2832, 2015.

[64] D. J. Shepphard, J. Powell, and S. C. Cripps, “An efficient broadband reconfigurable power amplifier using active load modulation,” *IEEE Microw. Wirel. Components Lett.*, vol. 26, no. 6, pp. 443–445, 2016.

[65] S.-H. Liao and Y. E. Wang, “High efficiency WCDMA power amplifier with pulsed load modulation (PLM),” *IEEE J. Solid-State Circuits*, vol. 45, no. 10, pp. 2030–2037, 2010.

[66] J. Jeong and Y. E. Wang, “Pulsed load modulation (PLM) technique for efficient power amplification,” *IEEE Trans. Circuits Syst. II Express Briefs*, vol. 55, no. 10, pp. 1011–1015, 2008.

[67] G. R. Nikandish, R. B. Staszewski, and A. Zhu, “Unbalanced power amplifier: An architecture for broadband back-off efficiency enhancement,” *IEEE J. Solid-State Circuits*, vol. 56, no. 2, pp. 367–381, 2020.

[68] S. Moloudi and A. A. Abidi, “The outphasing RF power amplifier: A comprehensive analysis and a class-B CMOS realization,” *IEEE J. Solid-State Circuits*, vol. 48, no. 6, pp. 1357–1369, 2013.

[69] P. Asbeck and Z. Popovic, “ET comes of age: Envelope tracking for higher-efficiency power amplifiers,” *IEEE Microw. Mag.*, vol. 17, no. 3, pp. 16–25, 2016.

[70] M. Alon, Y. Shor, A. Moshkin, T. Dagan, and S. Singer, “Envelope tracking power amplifier using short-time fourier transform,” *IEEE Microw. Wirel. Components Lett.*, vol. 31, no. 6, pp. 575–578, 2021.